

Forschungszentrum Karlsruhe

Technik und Umwelt

Wissenschaftliche Berichte

FZKA 6573

Two-level model for line radiation transfer in low Z target plasmas

B.N. Bazylev^{*}, H. Würz

Institut für Hochleistungsimpuls- und Mikrowellentechnik

Programm Kernfusion

^{*} permanent address: Minsk Heat and Mass Transfer Institute, 220072 Minsk, Belarus

This work partly was supported in the frame of the German WTZ cooperation agreement WEI-002-98 with Belarus

Forschungszentrum Karlsruhe GmbH, Karlsruhe

2001

Abstract

A two-level model describing He- and H-like ions by their ground state and one isolated excited level with collisional and radiative transitions between these levels and the continuum was developed. The model allows to take into account re-emission of line radiation when calculating line radiation transfer in plasmas with non uniform temperature and density distribution without solving detailed balance equations for level populations. For application of the two-level model in 1 dimensional line radiation transfer calculations several numerical schemes were developed and tested for a beryllium plasma. It is demonstrated that re-emission in the resonance lines increases the back radiated flux, the radiative flux to the target and the reradiated flux from the plasma cloud.

Zusammenfassung

Zwei Niveau Modell zur Berechnung des Transport von Linienstrahlung in niedrig Z Target Plasmas

Zur Berechnung des Transports intensiver Linienstrahlung He- und H-ähnlicher Ionen wurde ein einfaches Zwei Niveau Modell, bestehend aus Grundzustand, einem angeregten Niveau und dem Kontinuum, entwickelt. Stoß- und strahlungsinduzierte Übergänge zwischen verschiedenen Niveaus und dem Kontinuum werden berücksichtigt. Das Modell erlaubt die Berechnung der Re-Emission von Linienstrahlung in einem Plasma mit Dichte und Temperaturgradienten. Zur Anwendung des 2 Niveau Modells in 1-D Berechnungen des Linienstrahlungstransports wurden mehrere numerische Verfahren entwickelt und für ein Beryllium Plasma getestet. Reemission in Resonanzlinien He- und H-ähnlicher Ionen erhöht den zurückgestrahlten Strahlungsfluß, den Strahlungsfluß zum Target und die Abstrahlung von der Plasmawolke.

Content

1. Introduction	1
2. Description of the two-level model	2
3. Difference methods for the solution of the 1-D angular dependent radiation transfer equation	6
4. Discussion of numerical results	13
4.1. Optical properties of Be plasma.	13
4.2. Difference schemes for calculation of the 1-D radiation transfer.	16
4.3. Two level model with step function for temperature and density	19
4.4. Radiation transfer with two level model	22
5. Conclusions	24
6. References	25
Appendix 1	27

1. Introduction

Interaction of intensive hot plasma streams with peak power densities in the MW/cm^2 range with a solid surface produces target plasmas with non-uniform temperature and density distributions [1]. A cold, rather dense plasma, with temperatures of a few eV and densities of $10^{18} - 10^{19} \text{ cm}^{-3}$ is formed close to the target surface. In the region where the energy of incident hot plasma ions is absorbed a hot low dense plasma is formed. The plasma temperature there can achieve hundreds of eV, with densities being in the range $10^{14} - 10^{15} \text{ cm}^{-3}$. For graphite or beryllium as target material the plasma in the hot region is fully ionized and near the surface the degree of ionization of the plasma is close to one. A rather thin transition region with large temperature and density gradients connects these two regions. In this thin plasma layer the ionization of the plasma changes drastically from fully to weakly ionized plasma. The hot plasma region in spite of rather large spatial size is optically thin because of its low density. The transition region is also optically thin because of its rather small spatial size. For these reasons the intensity of continuum radiation, generated in both regions, is rather low and line radiation with a considerable fraction in the soft x-ray (SXR) energy region dominates there. Most of this radiation is radiated back from the plasma but part of it penetrates through the cold plasma and heats the target.

Intense line radiation from the high temperature plasma results in radiative excitation processes in the low temperature region. The line radiation from the high temperature plasma excites bound electrons and increases the population of the excited level of the corresponding transition if the ion exists in both temperature regions. Otherwise the line radiation is absorbed by free electrons and heats them or is absorbed by bound electrons resulting in ionization. Due to this additional excitation the population of excited levels increases. The additionally excited electrons are deexcited by collisions with free electrons resulting in electron heating and spontaneous radiative decay. Due to this spontaneous decay the emissivity of such lines can exceed the local thermodynamic equilibrium (LTE) emissivity corresponding to the local plasma temperature. The additional excitation can penetrate rather deeply into the cold plasma. In this case the total radiative flux could become larger. This effect can be very important for the lines of He-like ions because they exist over a rather large temperature interval, which for carbon extends from 4 eV up to 100 eV and for beryllium from 1.5 eV up to 50 eV. Therefore He-like ions are present in most regions of the target plasma and line

radiation from the rather hot region can change the level populations of He-like ions in the total volume of the cold plasma. For a realistic estimation of the target heat loads the penetration of this line radiation through the cold rather dense plasma has to be investigated.

The usual multi-group approach with opacities cannot describe adequately the line radiation transport through a non-uniform plasma from the hot to the cold region. Only a self-consistent radiative transfer model where all the processes of level population are taken into account together with solving the radiation transport problem is able to describe this situation adequately. The self-consistent approach means solution of the system of kinetic equations describing the level populations of all the ions together with radiation transfer equations in each time step. Such an approach is too bulky to be used in 2-D radiative transfer calculations. Therefore a two-level model was developed. In this model the radiative transfer in the continuum and for weak lines is calculated in the usual way by use of multigroup opacities. These are obtained from the collisional-radiative equilibrium (CRE) model with escaping factor corrections taking into account re-absorption of line radiation in non-LTE plasmas [2]. The radiative transfer in strong lines is calculated using a two-level model for the reemission of absorbed energy and the amount of energy transferred to free electrons in collisional transitions from the excited levels is estimated.

2. Description of the two-level model

The local radiation properties of a plasma are described by absorption $\kappa_{\mathcal{E}}$ and emission $J_{\mathcal{E}}$ coefficients. The absorption coefficients are determined by the population of the lower states and by free electrons. The emission coefficients are connected with populations of the upper (excited) states. In the LTE model all the excited levels are populated in accordance with the Boltzman equation corresponding to optically thick plasma. with equilibrium between radiation and level populations. In the CRE model collisional processes, spontaneous radiative decay between excited levels and between excited levels and the ground state, and di-electron recombination are taken into account. The influence of the plasma radiation on the level populations (processes of the radiation excitation, ionization, and induced deexcitation) is neglected. Level populations are obtained from the system of the balance equations connecting the level populations of ions and free electrons by the above-mentioned transitions. In the CRE model with

escaping factor correction the influence of the plasma radiation on the population of excited levels is taken into account by means of introduction of a special factor (escaping factor) which decreases the velocity of the spontaneous radiative decay. Thus the escaping factor describes re-absorption of line radiation in a plasma layer of finite size [3]. The escaping factors are defined for plasma layers of constant temperature and density. Thus for all the above mentioned models the absorption and emission coefficients correspond to local temperatures and densities of the plasma and the non local character of the radiation in optically transparent plasma is not taken into account.

For plasma ions with excited levels close to the continuum and far away from the ground state the influence of radiation on the level population can be approximately described by a two-level model. This model is based on the following assumptions: transitions occur only between the ground state and the excited level and the excited level and the continuum. Electron transitions between excited levels are neglected. A detailed calculation of level populations is not necessary, because of the high energy of the first excited level and the rather large energy intervals between the neighboring excited levels. Therefore there is no correlation between different lines and each line can be described separately. This model is applicable to He and H like ions of low Z materials such as beryllium and carbon. Figs. 1 a and b show the energy level structure of He-like and H-like ions of beryllium and carbon.

Radiation transfer within isolated lines at given temperature and density profiles is considered. The change of the radiation intensity I_ε along the length dl at the given frequency ε is given according to:

$$dI_\varepsilon = -\kappa_\varepsilon I_\varepsilon dl + J_\varepsilon dl + \tilde{J}_\varepsilon dl \quad (1)$$

The first term at the right side of the expression $\kappa_\varepsilon I_\varepsilon dl$ describes the absorption of the radiation at the given frequency, the second $J_\varepsilon dl$ the local plasma emissivity at the given frequency. The third term $\tilde{J}_\varepsilon dl$ is the re-emission of the absorbed energy within the line of given shape. Thus the radiation transfer equation can be written in the following form:

$$\frac{dI_\varepsilon}{dl} = -\kappa_\varepsilon I_\varepsilon + J_\varepsilon + \tilde{J}_\varepsilon \quad (2)$$

All terms except \tilde{J}_ε are known. \tilde{J}_ε can be defined as ratio between energy re-emitted (due to spontaneous decay and induced radiative de-excitation) and absorbed at the given frequency within the full line. The energy absorbed within the line can be re-radiated at any frequency within the line with the probability given by the line contour. This assumption of complete redistribution in the line is used in the two-level model.

The normalized line shape is assumed to have a Voigt contour $\Phi(\varepsilon)$ with the absorption coefficient κ_0 in the line center [4]. The total absorbed energy F per unit length l within the line is given as:

$$F = \int_{4\pi} d\Omega \int_0^\infty \kappa_0 \Phi_\varepsilon I_\varepsilon d\varepsilon \quad (3)$$

The absorbed energy from the excited level m to the ground state l is redistributed by several ways. A part of the energy is re-radiated by spontaneous radiative decay with the rate A_{m1} , and by induced radiative de-excitation with the rate B_{m1} . A part of the energy is used for heating of free electrons resulting in collisional de-excitation with the rate V_{m1}^{ZZ} and collisional ionization with the rate $V_{m1}^{Z,Z+1}$. A part of the energy is used for radiative ionization from the excited level with the rate $\nu_{m1}^{Z,Z+1}$.

Re-emission by spontaneous decay Ψ_s is given by the ratio of the transition frequency for spontaneous decay and the sum of all transition processes described by their transition frequencies. Ψ_s thus is given according to:

$$\Psi_s = \frac{A_{m1}}{A_{m1} + \nu_{m1}^{Z,Z+1} + B_{m1} + (V_{m1}^{Z,Z+1} + V_{m1}^{ZZ})N_e} \quad (4)$$

Re-emission by induced radiative de-excitation Ψ_i in analogy to eq. (4) is given as:

$$\Psi_i = \frac{B_{m1}}{A_{m1} + \nu_{m1}^{Z,Z+1} + B_{m1} + (V_{m1}^{Z,Z+1} + V_{m1}^{ZZ})N_e} \quad (5)$$

with N_e the density of the free electrons.

Assuming complete redistribution in the line and isotropic emission the re-emission term \tilde{J}_ε can be written in the following form:

$$\tilde{J}_\varepsilon = \frac{1}{4\pi} F \cdot (\Psi_s + \Psi_i) \cdot \Phi(\varepsilon) \quad (6)$$

The energy transferred to the free electrons in the collisional transitions E_{ct} can be estimated by the same way

$$E_{ct} = \frac{V_{m1}^{ZZ}}{A_{m1} + v_{m1}^{Z,Z+1} + B_{m1} + (V_{m1}^{Z,Z+1} + V_{m1}^{ZZ}) N_e} F \quad (6a)$$

For the velocities of the processes occurring in equations (4) and (5) well-known analytical expressions are used [3,5]. For the rate of the spontaneous radiative decay from the excited level m to the ground state the following expression is used:

$$A_{m1} = \frac{2E_{m1}^2 e^2}{m_e \hbar^2 c^2} f_{m1} = 4.35 \cdot 10^7 E_{m1}^2 f_{m1} \quad (7)$$

with f_{m1} the oscillator strength and E_{m1} the transition energy. Collisional excitation and de-excitation are connected by a detailed balance equation.

$$g_m V_{m1} = g_1 V_{1m} \exp\left(\frac{E_m - E_1}{T_e}\right) \quad (8)$$

The rate of the collisional de-excitation is described by the Meve formula.

$$V_{m1}^{ZZ} = 1.58 \cdot 10^{-5} \frac{f_{m1}}{E_{m1} \sqrt{T}} \left[A + C x_{m1} + (B x_{m1} - C x_{m1}^2 + D) \left(\ln \frac{1 + x_{m1}}{x_{m1}} - \frac{0.4}{(1 + x_{m1})^2} \right) \right] \quad (9)$$

Here $x_{m1} = E_{m1} / T_e$ and A, B, C, D are the approximation parameters with $A=0.15, B=C=0, D=0.28$ for the transitions in He- and H- like ions with $\Delta n \geq 1$. For collisional ionization the Lotz formula is used.

$$V_{m1}^{Z,Z+1} = 5.3 \cdot 10^{-8} \left(\frac{Ry}{T_e} \right)^{3/2} \mu_m E_i(-x_m) / x_m, \quad (10)$$

where $x_m = I_m / T_e$ with I_m the ionization potential from the excited level m , μ_m – the number of equivalent electrons at the level m and $E_i(-x_m)$ the exponential integral [6].

For the induced de-excitation and photo ionization the following expressions are used:

$$B_{m1} = \frac{g_1}{g_m} \int_{-\infty}^{\infty} \frac{\sigma_{1m}(\varepsilon) I_\varepsilon}{\varepsilon} d\varepsilon \quad (11)$$

$$V_{m1}^{Z,Z+1} = \int_{4\pi} d\Omega \int_{\varepsilon_m}^{\infty} \frac{\sigma_f(\varepsilon) I_\varepsilon}{\varepsilon} d\varepsilon \quad (12)$$

Here $\sigma_{1m}(\varepsilon)$ is the photo-excitation cross section per energy interval from the ground state, $\sigma_f(\varepsilon)$ is the photo-ionization cross-section from the excited level, ε is the photon energy, I_ε is the radiation intensity, g_1 , g_m are the statistical weights of the ground state and the excited level.

The photo-excitation and photo-ionization cross sections are obtained by using Hartree-Fock-Slater (HFS) calculations performed with TOPATOM [2].

3. Difference methods for the solution of the 1-D angular dependent radiation transfer equation

Two main approaches exist for calculation of radiation transfer in a plasma: solution of the radiation transfer equation either in the differential form or in the integral form. Each of them has some advantages and disadvantages. The local character (in the difference scheme quantities are related to mesh knots) is the main advantage of the differential radiation transfer equation. Due to this the calculational procedure is rather simple. Its main lack is that there is no simple way to build the difference schemes giving the correct limits both for optically thin and optically thick plasmas. In 1-D geometry most of the difference schemes give the correct limit for optically thin plasma. The non-local character of the integral radiation transfer equation means the following: the

calculated value in a mesh is connected not only with known values related to the mesh but with values related to surrounding meshes. The non-local character can be rather easy overcome for one-dimensional plane geometry. The main advantage of the integral radiation transfer equation is that most of the difference schemes give the correct limits both for optically thin and for optically thick plasmas. Below the difference schemes for both cases are described.

The differential form of the radiation transfer equation in analogy to eq. (2) is given as:

$$\mu \frac{dI_\varepsilon}{dx} = -\kappa_\varepsilon I_\varepsilon + J_\varepsilon + \tilde{J}_\varepsilon \quad (13)$$

with the following relationship between the path element dl and the x coordinate:

$$dl = \frac{dx}{\mu}, \quad \mu = \cos\theta$$

Here θ is the angle between the x -axis and the direction of the photon motion (polar angle).

The integral form of the radiation transfer equation is given as:

$$I_\varepsilon(l) = I_\varepsilon(0) \exp(-\kappa_\varepsilon l) + \int_0^l J_\varepsilon \exp\left(-\int_{l''}^l \kappa_\varepsilon dl'\right) dl'' + \int_0^l \tilde{J}_\varepsilon \exp\left(-\int_{l''}^l \kappa_\varepsilon dl'\right) dl'' \quad (14)$$

with the same relationship between l and x .

The total radiation flux S is calculated by integration over the space angle Ω and the photon energy ε .

$$S = \int_{4\pi} \Omega d\Omega \int_0^\infty I_\varepsilon d\varepsilon \quad (15)$$

To get the difference scheme for both cases the space coordinate x is divided by N non-uniform meshes of mesh size $\Delta x_{j+1/2} = x_{j+1} - x_j$. Angular grids are defined separately for positive ($\mu > 0$) and negative ($\mu < 0$) directions. $x=0$ is the left boundary of the plasma layer, $x=X_0$ its right boundary. Δl , Δx and μ are connected according to (the index i refers to the angular grid):

$$\Delta l_{j+1/2,i} = \Delta x_{j+1/2} / |\mu_i| \quad (16)$$

Radiative intensities are given at the mesh boundary; temperatures and densities of the plasma are given in the mesh center. The mesh boundary through which a photon enters a mesh is named incoming photon boundary. The mesh boundary through which a photon leaves a mesh is named outgoing photon boundary. A mesh $\{j+1/2\}$ has the left side boundary $\{x_j\}$ and the right side boundary $\{x_{j+1}\}$. For the negative direction of the photon propagation ($\mu < 0$) $\{x_{j+1}\}$ is the incoming photon boundary and $\{x_j\}$ is outgoing photon boundary. For the positive direction of the photon propagation ($\mu > 0$) $\{x_j\}$ is the incoming photon boundary and $\{x_{j+1}\}$ is the outgoing photon boundary. Let positions (0) and (Δl) in the difference schemes indicate the incoming photon and outgoing photon mesh boundaries for an arbitrary mesh.

Using these definitions the final expressions for the outgoing radiative intensity $I(\Delta l)$ can be written for the differential and the integral radiation transfer equation for an arbitrary mesh $\{j+1/2\}$. Here $\Delta l \equiv \Delta l_{j+1/2,i}$, the index i refers to the angular grid, the index j to the space grid.

For equation (13) the difference scheme is written in the following form:

$$I_\varepsilon(\Delta l) = \frac{\Delta l (J_\varepsilon(\Delta l) + \tilde{J}_\varepsilon(\Delta l)) + I_\varepsilon(0)}{1 + \kappa_\varepsilon \Delta l} \quad (17)$$

The source terms and the absorption coefficient are defined at the mesh boundaries Thus eq. (17) can be written according to:

$$\begin{aligned}
I_{\varepsilon,j+1,i} &= \frac{\Delta l_{j+1/2,i} (J_{\varepsilon} + \tilde{J}_{\varepsilon})_{j+1,i} + I_{\varepsilon,j,i}}{1 + \kappa_{\varepsilon,j+1} \Delta l_{j+1/2,i}}, & \mu_i > 0 \\
I_{\varepsilon,j,i} &= \frac{\Delta l_{j+1/2,i} (J_{\varepsilon} + \tilde{J}_{\varepsilon})_{j,i} + I_{\varepsilon,j+1,i}}{1 + \kappa_{\varepsilon,j} \Delta l_{j+1/2,i}}, & \mu_i < 0
\end{aligned} \tag{17*}$$

Eq. (17) describes the S_N method. The photon path Δl_i , the cosine μ_i and the mesh size Δx are connected by eq. (16).

For eq. (14) the difference scheme can be derived assuming that the source terms ($J_{\varepsilon}, \tilde{J}_{\varepsilon}$) either are constant within the mesh or linearly dependent on the optical length. For constant source terms within the mesh the difference scheme can be written in the following form:

$$\begin{aligned}
I_{\varepsilon}(\Delta l_i) &= I_{\varepsilon}(0) \cdot \exp(-\tilde{\kappa}_{\varepsilon} \Delta l_i) + \frac{1}{\tilde{\kappa}_{\varepsilon}} \left(J_{\varepsilon} \left(\frac{\Delta l_i}{2} \right) + \tilde{J}_{\varepsilon} \left(\frac{\Delta l_i}{2} \right) \right) (1 - \exp(-\tilde{\kappa}_{\varepsilon} \Delta l_i)) \\
\tilde{\kappa}_{\varepsilon} &= \frac{1}{2} (\kappa_{\varepsilon}(0) + \kappa_{\varepsilon}(\Delta l_i)), \quad \Delta l_i = \Delta x / |\mu_i|
\end{aligned} \tag{18}$$

here the source terms J_{ε} and \tilde{J}_{ε} are defined at the mesh center where the initial temperatures and densities are defined. The photon path Δl_i , the cosine μ_i and the mesh size Δx are connected by eq. (16).

Using eq. (14) and the assumption of linear dependence of the source terms J_{ε} and \tilde{J}_{ε} on the optical length $\tau = \kappa_{\varepsilon} \Delta l$ within the mesh the difference scheme can be written in the following form:

$$\begin{aligned}
I_{\varepsilon}(\Delta l_i) &= I_{\varepsilon}(0) \cdot \exp(-\kappa_{\varepsilon}(\Delta l_i) \Delta l_i) + \frac{1}{\kappa_{\varepsilon}(\Delta l_i)} (J_{\varepsilon}(\Delta l_i) + \tilde{J}_{\varepsilon}(\Delta l_i)) \times \\
&\times \left(1 - \frac{1 - \exp(-\tilde{\kappa}_{\varepsilon} \Delta l_i)}{\tilde{\kappa}_{\varepsilon} \Delta l_i} \right) + \frac{1}{\kappa_{\varepsilon}(0)} (J_{\varepsilon}(0) + \tilde{J}_{\varepsilon}(0)) \cdot \left(\frac{1 - \exp(-\tilde{\kappa}_{\varepsilon} \Delta l_i)}{\tilde{\kappa}_{\varepsilon} \Delta l_i} - \exp(-\tilde{\kappa}_{\varepsilon} \Delta l_i) \right), \tag{19} \\
\tilde{\kappa}_{\varepsilon} &= \frac{1}{2} (\kappa_{\varepsilon}(0) + \kappa_{\varepsilon}(\Delta l_i)), \quad \Delta l_i = \Delta x / |\mu_i|
\end{aligned}$$

here κ_{ε} , J_{ε} , \tilde{J}_{ε} refer to the mesh boundaries. The photon path Δl_i , the cosine μ_i and the mesh size Δx are connected by eq. (16).

As soon as the values κ_ε , J_ε , \tilde{J}_ε are determined for the given boundary conditions at both surfaces of the plasma layer the intensities can be calculated for all meshes and angles as described below. Let $I_\varepsilon(\mu_i) = I_{r\varepsilon}^0(\mu_i)$ be the boundary condition at the right surface ($x=X_0$) for $\mu < 0$ and $I_\varepsilon(\mu_i) = I_{l\varepsilon}^0(\mu_i)$ the boundary condition at the left surface ($x=0$) for $\mu > 0$. Thus starting from the mesh number N the outgoing intensities at the left mesh boundary are used as the incoming intensities $I_{r\varepsilon}^0(\mu_i)$ for negative μ_i . Using these values the outgoing intensities for the mesh number N-1 are obtained and so on till the mesh number 1. After obtaining the outgoing intensities at the left surface of the plasma layer the same procedure is performed to calculate the outgoing intensities in the positive directions μ_i for all the meshes starting from mesh number 1 using $I_{l\varepsilon}^0(\mu_i)$ as the incoming intensities for this mesh. The numerical procedure is the same for the eqs. (17) - (19).

The total spectral radiation flux S_ε and spectral radiation fluxes S_ε^- in negative direction ($\mu < 0$) and S_ε^+ in positive direction ($\mu > 0$) are obtained by integration over μ :

$$S_\varepsilon = \sum_{\mu_i < 0} \mu_i I_\varepsilon(\mu_i) A_i + \sum_{\mu_i > 0} \mu_i I_\varepsilon(\mu_i) A_i = S_\varepsilon^- + S_\varepsilon^+ \quad (20)$$

with A_i the weights of for instance the Gaussian quadrature formula.

Performing the calculations for all energy groups and integrating over the photon energy the radiative flux $S(x_j)$ is obtained for all meshes according to:

$$S = \sum_{\varepsilon} S_\varepsilon \Delta \varepsilon \quad (21)$$

For deriving the difference expressions (17) and (19) it was assumed that the absorption and emission coefficients κ_ε , J_ε , \tilde{J}_ε refer to the mesh boundaries. Temperature and density are given in the mesh center. Only in this case the difference approximation of the radiation transfer equation (as shown in [7]) gives the correct limit of the radiative flux S for an optically thick plasma: $S \sim -dB/d\tau$ (B is the Planck function) [8]. This limit follows directly from the diffusion radiation transfer equation:

$$\kappa_\varepsilon S_\varepsilon = -cg^2 \frac{\partial U_e}{\partial x} \quad (22)$$

with U_e the radiation energy density, c the speed of light, g^2 the Eddington factor, which is equal to $1/3$ for isotropic radiation. Assuming $\tau_\varepsilon = \kappa_\varepsilon x \rightarrow \infty$ results in a weakly anisotropic radiation and in blackbody density U_ε^{Pl} of the radiation energy in the plasma. Thus eq. (22) can be rewritten as:

$$S_\varepsilon = -\frac{c}{3} \frac{\partial U_\varepsilon^{Pl}}{\partial \tau_\varepsilon} \quad (23)$$

U_ε^{Pl} is given as $U_\varepsilon^{Pl} = \frac{1}{c} \int_{4\pi} B_\varepsilon d\Omega = \frac{4\pi}{c} B_\varepsilon$ with the B_ε Planck function. After substitution into eq. (23) it is obtained:

$$S_\varepsilon = -\frac{4\pi}{3} \frac{\partial B_\varepsilon}{\partial \tau_\varepsilon} \quad (24)$$

No simple difference schemes exist satisfying the correct limit for optically thick plasma if the absorption and emission coefficients are given at the mesh center. For optically thin plasmas the above-described schemes are automatically fulfilled. The asymptotic behavior of all the above-described difference schemes for the case of optically thick plasma is investigated in Appendix 1. It is not necessary to assume that all these values are identical from the left and the right side of a mesh boundary (they relate to different meshes). For instance $\kappa_{j,\varepsilon}^+$ (right side value for boundary $\{j\}$) can be different from $\kappa_{j,\varepsilon}^-$ (left side value). For the boundary $\{j\}$ the right side value relates to the mesh $\{j+1/2\}$ and the left side value relates to the mesh $\{j-1/2\}$. Hence in eqs. (17) and (19) all the terms defined at the mesh boundaries ($\kappa_\varepsilon, J_\varepsilon, \tilde{J}_\varepsilon$) are determined by the calculated mesh and direction of the calculation. For negative μ the incoming values have to be taken as left side ones and the outgoing values as right side ones. For positive μ the incoming values have to be taken as right side ones and the outgoing values as left side ones.

For determination of κ_ε , J_ε , \tilde{J}_ε at the mesh boundaries a two-step procedure is used. At the first step preliminary values of temperatures are defined at the mesh boundaries and at the second step the final values of temperatures are obtained. For calculation of preliminary temperatures the number of meshes is doubled. Each mesh is divided into two equal parts. For the boundary temperatures of the new meshes whose boundaries coincide with the centers of the old meshes the old center temperatures are used. For these boundaries the temperatures from left and right sides are equal. For the other mesh boundaries three temperatures are calculated: the first is the result of an interpolation between the neighboring meshes, the second one is the result of an extrapolation from the left neighboring meshes and the third one is the result of an extrapolation from the right neighboring meshes. Then for the right side temperature the minimum between the interpolated value and the right side extrapolated value is chosen and for the left side temperature the minimum between the interpolated value and the left side extrapolated value is chosen. Therefore for these mesh boundaries the left side temperature must not coincide with the right side one. The densities at the mesh boundaries of the doubling mesh grid are obtained by simple interpolation.

At the second step temperatures are recalculated to conserve the total integral over each old mesh as described. For each old mesh the values $T_{j+1/2}\Delta M_{j+1/2}$ have to be conserved ($\Delta M_{j+1/2}$ is the mass in the mesh). The integral is calculated for each old mesh and for the two new meshes produced from it. Then the boundary temperatures are multiplied by a factor having the ratio of these integrals to get the final boundary temperatures. Then κ_ε , J_ε , \tilde{J}_ε are determined using the boundary values of temperature and density.

The new doubled mesh grid is used for radiation transfer calculation. This method was tested and showed good agreement with analytical solutions for a wide range of the optical thickness of the plasma layer from optically thin up to optically thick case [7].

For radiative transfer calculations it is more preferable to use the integral form instead of the differential form for the following reasons: the integral form of radiation transfer equation describes the radiation transport more correctly for the cases of large or optically thick meshes. Also in the case of large temperature and density gradients the linear integral method gives radiative fluxes with reasonable accuracy for rather rough meshes. Moreover for the integral form it is easier to take into account non-constant

distributions of source functions along a mesh, a fact being rather important for the radiation transfer in lines using the two-level model.

For all the above mentioned difference schemes the forward-reverse approximations can be obtained if the number of angles in each hemisphere is reduced to 1 and if μ is taken as $\mu = \frac{1}{2}$ for the positive direction and $\mu = -\frac{1}{2}$ for the negative direction.

For the calculation of the radiation transfer in resonance lines by the two-level model the Λ iteration procedure [9] is used. For increasing the stability and the velocity of convergence the iteration parameter Λ is chosen for each line separately. In Λ iteration the final value after iteration is taken as the sum of the value obtained from the difference equations (preliminary value) with weight Λ and the value from the previous iteration with weight $(1-\Lambda)$. ($0 < \Lambda \leq 1$). At $\Lambda=1$ the final value coincides with the preliminary calculated value and at Λ close to 0 the preliminary calculated value becomes a small correction to the value from the previous iteration. This method is used for non-monotonic convergence.

4. Discussion of numerical results

Radiation transfer calculations were performed for beryllium plasmas using two sets of Planck opacities: with 254 and with optimized 461 spectral groups. The optical properties of the beryllium plasma were obtained from TOPATOM [2] using the CRE model with escaping factors for a plasma layer of thickness $L=1$ cm. The spectral groups were chosen to describe as close as possible the features of the spectral radiation flux. If it is not mentioned separately in each hemisphere 16 Gaussian distributed angular directions were used. For the calculations of the line transfer with the two level model the Voigt line contour was used for the He-like lines and either Holtzmark or Voigt line contours were used for the H-like lines. The Holtzmark line contour was applied for the main transition in H-like ion.

4.1. Optical properties of Be plasma.

The steady-state CRE model was used for the calculation of the absorption and emission opacity tables of the beryllium plasma. In this model ion concentrations and level populations are obtained from the system of the steady-state balance equations. The

number of balance equations in the system corresponds to the total number of the energy levels of all ions taken into account in the calculations. For an arbitrary level i of an ion of charge m the balance equation is written in the following way:

$$-\sum_j N_i^m K_{ij}^m - N_i^m K_i^m + \sum_j N_j^m K_{ji}^m + \sum_j N_j^{m-1}(i) K_j^{m-1} + \sum_j N_j^{m+1}(i) K_j^{m+1} = 0$$

with N_i^m - the population of the level i of an ion of charge m ; N_j^m - the population of the level j of an ion of charge m ; $N_j^{m-1}(i)$ - the population of the level j of an ion of charge $m-1$; $N_j^{m+1}(i)$ - the population of the level j of an ion of charge $m+1$; K_{ij}^m - the velocity of the collisional and radiative transition from the level i to the level j ; K_{ji}^m - the velocity of the collisional and radiative transition from the level j to a level i ; K_j^{m-1} - the velocity of ionization from the level j of an ion of charge $m-1$; K_j^{m+1} - the velocity of recombination on the level j of an ion of charge $m+1$; K_i^m - the velocity of ionization from the level i of an ion of charge m .

The first term in the balance equation describes the decrease of the population of the level i due to collisional excitation to the upper levels and collisional and radiative deexcitation to the lower levels. The second term describes the decrease of the level population due to collisional ionization. The third term describes the increase of the population of the level i due to collisional excitation from the lower levels j and collisional and radiative deexcitations from the upper levels j . The fourth term describes the increase of the population of the level i due to the ionization to the desired configuration from the ion of the lower rate of ionization. The fifth term describes the increase of the population of the level i due to recombination to the desired configuration from the ion of the higher charge.

The following processes were taken into account: electron excitation and de-excitation, impact ionization, three-body recombination, spontaneous emission and photo and dielectronic recombination [5]. The velocities of the collisional transitions from the ground states were calculated using either the Born or the Born-Coulomb approximations [5]. The Van Regemorter expression was used for the collision transitions between excited levels and the Lotz expression - for the impact ionization. The Berdges

expression was used for dielectronic recombination and HFS calculated velocities for the spontaneous transitions and the photo-recombination.

The processes of radiation excitation and ionization are not usually taken into account in the framework of the CRE model because the increase of the excited level population due to absorption inside the resonance lines is larger than due to radiative excitation by the continuum radiation. Therefore the influence of the continuum radiation is not so important. The influence of the own plasma radiation on the excited level population can be taken into account by use of escaping factors which describes the decrease of the spontaneous decay velocity due to self-absorption of lines [3]. The escaping factor depends on the optical thickness in the center of a line and on the line shape. In case of a non uniform temperature and density profile the escaping factor can be obtained from a solution of the Biberman-Holstain equation. For a plasma layer with constant temperature and density the escaping factor Θ_{ij} can be expressed by the simple analytical formula:

$$\begin{aligned}\Theta_{ij} &= 0.67 / \sqrt{\pi\eta} && \text{for the Lorentz line shape} \\ \Theta_{ij} &= 0.5 / \eta \sqrt{\pi \ln \eta} && \text{for the Doppler line shape} \\ \Theta_{ij} &= 0.22 / \eta^{3/5} && \text{for the Holtzmark line shape}\end{aligned}$$

with $\eta = \kappa_0 L$, κ_0 - the absorption coefficient in the line center and L – the thickness of the plasma layer. The spontaneous decay velocity for each line is multiplied by the appropriate escaping factor in the system of balance equations.

In the calculation of the optical properties of beryllium plasma the escaping factors were taken into account for all the lines (with different kinds of line shapes) assuming that the thickness of the plasma layer is equal to 1 cm.

Absorption and emission coefficients of beryllium plasma for different plasma temperatures and densities of 10^{17} and 10^{18} cm^{-3} are shown on Figs. 2 a-g. The absorption and emission coefficients within the high frequency region between 100 and 200 eV which corresponds to the main lines of the He-like and the H-like ions are shown on Figs. 3 a and b for a plasma density of 10^{17} cm^{-3} and two temperatures - 10 eV (a) and 32 eV (b). From these figures the following conclusions are drawn: He-like ions exist in the

rather wide temperature region at least from 2 eV up to 50 eV (see Fig.2). In the low and intermediate frequency region the absorption coefficient practically coincides with the emission one i.e. equilibrium between absorption and emission exists (excited levels are populated according to equilibrium conditions LTE). In the high frequency region (He-like and H-like ions) this equilibrium is violated and the emission coefficient becomes lower than the absorption coefficient (for resonance lines also (see Figs. 3 a and b)). This is due to the following: for the H- and He-like ions the velocities of the spontaneous decay from excited levels (corrected by self-absorption within the lines in the escaping factor assumption) are much higher than the velocities of the collisional excitation from the ground states and there is not enough radiation excitation from the ground state also. Therefore the populations of the excited levels are much lower than the equilibrium populations. The degree of non-equilibrium in the high frequency region (difference between absorption and emission coefficients) increases with increasing temperature and decreasing density. The He-like lines are placed rather far from the Li-like threshold from the ground state. Therefore the continuum radiation cannot significantly influence the excited level population of these lines. For the H-like lines, which are located in the vicinity of the He-like threshold from the ground state the intensity of continuum radiation is rather high. This can increase the excited level populations of the H-like ions.

Thus in the plasma with non-uniform temperature and density the population of the excited levels of the He-like ions can be increased by excitation due to line radiation from the high temperature plasma region and excited level populations of the H-like ions can be increased by the continuum radiation from the He-like threshold. These processes cannot be described by the escaping factor model and must be described by special theoretical models as for instance the two level model.

4.2. Difference schemes for calculation of the 1-D radiation transfer.

For checking the accuracy of the used difference schemes and the adequacy of mesh resolution numerical calculations with different spatial resolutions of the given temperature and density profile were performed for a beryllium plasma layer. Typical temperature and density profiles in the beryllium plasma as used in the calculations are presented on Figs. 4 and 5. For the given temperature and density profile the three methods 1-D S_N (eq. (17)), linear integral method (eq. (19)) and constant integral method

(eq. (18)) were used for calculation of the radiation transport. For the optical properties Planck opacities were used.

Figs. 4 and 5 show the initial temperature and density profile as solid curves with 16 meshes (giving rather rough space resolution of the transition region) and as dashed curves with 64 meshes produced by adding additional meshes. The new meshes are implemented mainly in the region with large temperature and density gradients.

Calculated total radiation fluxes and fluxes in the positive and negative direction are shown in Figs. 6-8 for the initial profile and in Figs. 9-11 for the adequately resolved profile. In these figures the solid curves show the radiative fluxes obtained by using eq. (17*) (S_N method), the dashed curves show the radiative fluxes obtained by using the integral method (eq. (19)) with linearly depending source terms within the mesh, the dotted curves show the radiative fluxes obtained by using eq. (18) with constant source terms related to the mesh center. Radiative fluxes for initial and adequately resolved profiles using the linear integral method are presented in Fig. 12.

An analysis of the character of the radiation generated in the different plasma regions can help to understand the numerical results. The low temperature plasma region close to the wall is optically thick due to its low temperature and its rather high density. Due to this the radiation fluxes close to the target in positive ($\mu > 0$) and negative ($\mu < 0$) directions are rather similar (compare Figs. 7 and 8, 10 and 11) and the spatial dependence of the one-side radiation fluxes repeats the spatial dependence of the plasma temperature (Fig. 4). This behavior is typical to near blackbody radiation. Because of rather high optical thickness the continuum radiation dominates in this region. The continuum radiation from this region contributes with about 30% to the back-radiated flux (see Fig. 7 and 8, 10 and 11). The hot plasma region is optically thin and a rather small amount of radiation is generated there (Figs. 7 and 8, 10 and 11). The main part of the back-radiated flux is generated in the vicinity of the transition region where the Li-like and He-like ions are the main ions (see the one side radiative fluxes in positive direction Figs. 7 and 10). Due to the rather small spatial size of the transition region and the fast drop of the plasma density this region is optically thin for continuum radiation and line radiation dominates here. A rather large amount of line radiation is generated in the transition region also in negative direction (Figs. 8 and 11), but due to the large optical thickness of the cold plasma this radiation is absorbed there and the rather cold plasma reradiates in the continuum. Such transformation of the spectral radiation flux in

the negative direction S^- due to its propagation from the transition region into the cold plasma is shown on Fig. 13 where the spectral radiation flux is plotted at several positions in the vicinity of the transition region.

From Figs. 6-11 it is seen that there are differences between the cases with adequately resolved mesh and the rough mesh related with convergence of the results obtained from the different schemes. For an adequately resolved mesh all the schemes give quite similar radiative fluxes in all the space points (see Figs. 9-11) whereas for the rough mesh rather large differences in the radiative fluxes (see Figs. 6-8) were obtained. The behavior of the calculated radiative fluxes using the two difference schemes S_N and linear integral methods with boundary determined source terms is similar. There is no difference in the radiative flux onto the wall and in the plasma region between the wall ($x=0$) and $x=3.5$ cm (the low temperature plasma region). Differences in the radiative fluxes appear in the transition region (sharp increase of the plasma temperature and decrease of the plasma density) and are up to 7%. In all the space points the radiative flux obtained by the linear integral method is greater than the radiative flux calculated by the S_N method. The integral difference scheme with constant source terms (eq. (18)) gives similar values of radiative flux onto the wall and close values of back radiated fluxes, difference being less than 3.5%. But there are large differences in the radiative flux inside of the plasma layer especially in the transition region. The differences amount up to 25% at the position $x=5$ cm and a factor of 3.5 at the position $x=3.5$ cm. This method gives a rather large radiative flux in the direction towards the low temperature plasma exceeding the correct value by a factor of 3.5 (see Fig. 6). Thus radiative cooling of the transition region and heating of the low temperature plasma are overestimated.

The reason for this large difference can be explained in the following way. In Appendix 1 it is shown, that difference schemes with source terms defined at the mesh centers incorrectly describe the energy exchange between neighboring meshes in optically thick plasmas. The radiation flux between meshes is proportional to the sum of two terms: the first of them is the difference between the Planckian functions (B) belonging to neighboring meshes ($S \sim B_{i-1/2} - B_{i+1/2}$) the second term is $(-\partial B/\partial \tau)$ -like term. (The correct asymptotic is the radiative flux has to be proportional to $-\partial B/\partial \tau$). The first term dominates in case of large temperature gradients therefore total radiation flux is overestimated significantly for such regions. In [7] it was shown for high-energy explosions that the incorrect energy exchange between meshes leads to a rather large

overestimation of the velocity of the radiation wave and to a rather quick cooling of the hot plasma. The influence of the non-correct additional term decreases with reducing the mesh size. Thus rather large differences in the radiation fluxes exist if rough spatial grids are used (Figs. 6-8). And the differences decrease for adequately resolved spatial grid (Figs. 9-11).

From the numerical calculations it follows that all the above-described methods can be used in combination with an adequately resolved mesh. The linear integral method and the differential method are suitable for radiation transfer calculations if a rough mesh is used. The linear integral method (eq. (19)) is more preferable in all the cases because it gives radiative fluxes with higher accuracy than the other methods both for the adequately resolved mesh and for the rough mesh (see Fig. 12).

The dependency of the radiative fluxes from the number of rays is investigated using two limiting cases: 1) forward-reverse method where full isotropy of radiation in each hemisphere is assumed; 2) good angular resolution with 16 rays in each hemisphere. The comparison was performed on the fixed profile with adequately resolved mesh for all the above described difference schemes. The total radiation fluxes and one-side fluxes in positive ($S(+)$) and negative ($S(-)$) directions are shown in Figs. 14 – 16. For all the difference schemes the radiative fluxes directed from the high temperature region towards the low temperature region are slightly overestimated by the forward-reverse method in the vicinity of large temperature gradients (see one-side radiative fluxes in negative direction in Figs. 14-16). The radiation fluxes in back direction as obtained by forward-reverse method are also higher in the optically thin high temperature region. Thus radiation is close to isotropy in the optically thick low temperature plasma region. In both cases the radiation intensities along axis are smaller than along inclined lines because along inclined lines optical thickness is greater. The differences between radiation fluxes obtained using different angular resolutions are not so high. Therefore the adequate angular resolution is not so important for the given temperature and density profiles.

4.3. Two level model with step function for temperature and density.

The main features of the two level model were investigated by use of artificial 3-step temperature and density profiles. Using such step profiles eliminates the influence of the transition zone where together with change of temperature and density ion

concentrations can drastically change. Highest and intermediate temperatures were chosen so that He-like ion existed at both temperatures. At the lowest temperature He-like ions are absent. At intermediate temperatures practically all the electrons of He-like ions are in the ground state. The highest temperature corresponds to practically equal concentrations of He- and H-like ions. The three temperature and density profiles as used in the test calculations are shown in Fig. 17,19,21 (temperature), and in Fig. 18,20,22 (density). These test profiles differ one from another by decrease of density of low temperature regions. The density in the high temperature region differs from that one in the intermediate temperature region by two order of magnitude for the first case, by one order of magnitude in the second case and is practically equal for the third case.

The linear integral method (as more accurate) was used in these test calculations. The higher accuracy is necessary for radiation transfer calculations because temperature and density discontinuity is present. The Λ iteration procedure converges rather quickly. It needs less about 15 iterations for each line. Calculated radiation fluxes (total fluxes and fluxes S^+ and S^-) are shown in Figs. 23,24 for the first test profile, in Figs. 27,28 for the second test profile, and in Figs. 31,32 for the third test profile. Initial and final results after 15 iterations using the two level model are plotted. The initial results are the results obtained using Plank opacities. For the demonstration of the anisotropy of the radiation average cosines in the positive μ^+ ($\mu > 0$) and in the negative μ^- ($\mu < 0$) direction are shown in Figs. 25,26, Figs. 29,30, and Figs. 33,34 for the same test profiles. The average cosines are defined according to:

$$\mu^+ = \frac{\int_0^\infty d\varepsilon \int_0^1 \mu I d\mu}{\int_0^\infty d\varepsilon \int_0^1 I d\mu}, \quad \mu^- = \frac{\int_0^\infty d\varepsilon \int_{-1}^0 \mu I d\mu}{\int_0^\infty d\varepsilon \int_{-1}^0 I d\mu}$$

Radiation can be assumed to be isotropic if the averaged cosines μ^\pm are equal to ± 0.5 . For the test cases in all regions radiation drastically differs from isotropy: $\mu^+ < 0.5$, $\mu^- > -0.5$. This is a typical situation for an optically thin plasma where radiation intensities under large angles to the x-axis dominate. The application of the two level model with amplification of line intensities only slightly changes the average cosines, i.e. the radiation flux remains significantly anisotropic.

The main features of test calculations with the two level model are presented below. The spatial distribution of the relative velocity of energy transfer to the free electrons by the collisional deexcitation given as V_{m1}^{zz} in eq. (9) and by spontaneous decay for the main He-like line (transition from the first excited level to the ground state) given as A_{m1} in eq. (7) are shown in Figs. 35-37. In the high temperature plasma re-emission by spontaneous decay is the main process. Collisional deexcitation of electrons competes with the spontaneous decay in the intermediate temperature region at rather high density (first case, Fig. 35). But with decrease of density re-emission by spontaneous decay dominates in all temperature regions where He-like ions are present (second and third cases, Figs. 36,37). Thus the additional excitation of the lines by radiation from the plasma region with higher temperature is practically spent for re-radiation and for maintaining populations on the excited levels at rather far distance from the high temperature region if the density of low temperature plasma is not so high. The additional excitation of the lines is partly spent for heating of free electrons if the plasma density is rather high and line intensity can damp rather quickly inside the cold plasma in this case. Calculated radiation fluxes in the lines (total fluxes and fluxes in the positive S^+ and negative S^- direction) are shown in Figs. 38,39 for the first test profile, in Figs. 40,41 for the second test profile, and in Figs. 42,43 for the third test profile. Initial and final results after 15 iterations are plotted. Despite of comparable total initial and final radiation fluxes in the low temperature region (see Figs. 23,27,31) there are difference in the initial and final line radiation fluxes because of excitation of ground state electrons by line radiation from the high temperature region. This fact is evident from the Fig. 44 showing the spectral radiation flux in the positive ($\mu > 0$) direction at the position $x=3.2$ cm for first test variant (in direction from low temperature region to high temperature region). This position corresponds to the intermediate temperature region close to the high temperature region. In the initial spectral radiation flux radiation in the He- and H-like lines is practically absent. After 15 iterations using two level model intensive radiation in these lines appears. The intensity of this line radiation practically equals the intensity of the line radiation in the negative direction at the same place (see Figs. 45,46). Amplification of the lines due to re-absorption is observed in the high temperature plasma too. Due to this the lateral leakage radiation from the plasma significantly increases (see Figs. 47-49). Here the lateral leakage radiation is calculated

as the angular integrated volumetric energy loss by a plasma of lateral width of 0.1 cm with constant lateral temperature. The significant increase of the lateral leakage radiation in the high temperature region is mainly due to a rather large amplification of one H-like line caused by continuum radiation from the He-like threshold. That is continuum radiation of the He-like threshold significantly increases the population of the excited levels of H-like ions. This is seen in Figs. 50 a and b where the lateral leakage spectral radiation fluxes and integrated lateral leakage radiation fluxes (defined as

$$S(\varepsilon) = \int_0^{\varepsilon} S_{\varepsilon'} d\varepsilon')$$

are shown for the first test profile at position $x=4$ cm for the opacity approach (initial) and the two level model. According to Fig. 50b the lateral leakage radiation is dominated by the two lines at 123.6 eV(He-like ion) and 162.4 eV (H-like ion).

Thus amplification of the line radiation in He- and H- like lines due to re-absorption of line radiation from the high temperature region increases with decreasing difference in the plasma densities of high and low temperature region. When spontaneous decay dominates in the low temperature region the influence of the line radiation from the high temperature plasma can penetrate up to a rather far distance inside of the low temperature plasma.

4.4. Radiation transfer with the two level model.

The test calculations showed that both the linear integral method and the differential method with good angular resolution can be used for calculations with the two-level model. The linear integral method is preferable because it gives a more accurate description of the re-emission term within the mesh. Therefore this method was used.

Calculations were performed with the temperature and density profiles as shown in Figs. 4, 5 using the adequately resolved mesh. Results (spectral radiation fluxes back radiated and to the wall) are shown in Figs. 51-54. The calculations were also performed for modified temperature and density profile of the beryllium plasma as shown in Figs. 55, 56. The profiles have steeper temperature and density gradients in the transition region. Calculated results are presented in Table 1 and in Figs. 57-60. The Λ iteration procedure converges rather quickly. It needs less than 20 iteration for each line. For these cases the two-level model was applied only for the resonance He-like lines.

From Figs. 4, 5, 55 and 56 it is seen that the plasma density decreases quickly between the transition region and the free surface of the expanding plasma, with the temperature being approximately constant. In this case the emissivities of lines decreases also between the transition region and the free surface. The maxima of the line emissivities are close to the transition region. The optical thickness of the plasma in the center of the resonance lines calculated from the transition region to the free surface are several orders of magnitudes. The region with optical thickness $\tau \approx 1$ calculated from the free surface determines the radiation outgoing from the plasma. In radiation transfer calculations with multigroup opacities where re-emission is not taken into account the outgoing intensity in the resonance lines is less than the maximum values due to absorption in the path from the transition region to the position with $\tau \approx 1$. For the two-level model taking re-emission of the absorbed radiation into account the outgoing intensity of lines increases and comes closer to the maximum value as can be seen from the calculated results.

These arguments are also valid for line radiation transport from the transition region through the cold dense plasma to the wall. But in this case due to the increase of the plasma density and decrease of the plasma temperature (see Figs. 5 and 6) the larger part of the absorbed energy is spent for heating of plasma electrons and not for re-emission. Therefore line intensity decreases more quickly than in the opposite direction.

From the back-radiated spectral flux (Figs. 51, 52, 57, and 58) it is seen that due to re-emission of absorbed radiation coming from the transition region the intensities of the resonance lines increase. Therefore the back-radiated flux increases also (see Table 1). From the spectral radiation flux onto the wall (Figs. 53, 54, 59, and 60) it is seen that only the intensity of the first resonance He-like line increases and the deep cutting of the line center is removed for both profiles. For the first temperature and density profile (Figs. 5 and 6) the second resonance He-like line also penetrates through the cold plasma to the wall (see Figs. 53 and 54).

Finally results of the radiation transport calculations using different opacity approaches are compared in Table 1. The fixed temperature and density profiles from Figs. 55 and 56 were used in these calculations. Radiation transfer calculations with multi-group Rosseland opacities describe only continuum radiation. Calculations with multi-group Planck opacities take line radiation into account but neglect re-emission.

In the opacity approaches the radiation heat flux to the wall is determined by the continuum radiation. Penetration of the resonance lines through the cold plasma due to re-emission increases the target heat load significantly. The back radiation flux is determined by line radiation and taking into account re-emission in the resonance line increases the value at least by 10%.

5. Conclusions

Calculations with different schemes for the radiation transfer equation have shown that the radiation fluxes calculated with the linear integral scheme are only weakly dependent on the used spatial grid. Therefore this scheme is preferable. The two-level model developed for radiation transfer in strong lines allows taking into account re-emission of the line radiation in plasmas with non uniform temperature profiles without performing detailed calculations of level populations. The radiation transfer calculations for given temperature and density profiles show that amplification of the line radiation in He- and H- like lines due to re-emission of line radiation from the high temperature region increases with decreasing difference in the plasma densities of low temperature and high temperature plasma regions. The radiation transfer calculations with a given temperature and density profile in a beryllium plasma shield show that taking into account re-emission in the resonance lines of He- and H- like ions increases the back radiated flux at least by 10% and the radiative flux to the target by about 30%.

Test calculations show that the continuum radiation of the He-like threshold significantly increases the excited level populations of H-like ions. This leads to an increase of the line radiation from the hot plasma region.

The opacities obtained using the CRE model with escaping factor take into account the influence of the plasma radiation on the level populations under the following assumptions only: no influence of continuum radiation on the level populations, re-absorption of the line radiation increases the population of excited levels by means of multiplication of the velocity of spontaneous decay by escaping factor, constant temperature and density profile inside a plasma layer of fixed size is supposed for obtaining the escaping factor. The two level model allows to overcome these restrictions.

6. References

1. Würz H. et al., Fusion Technology 32 (1997) 45.
2. V.Tolkach, H.Würz. TOPATOM code for calculation of optical properties of plasma using CRE model. FZKA report to be published.
3. Derziev V.I., Zidkov A.G., Jakovlenko S.I. Radiation in nonequilibrium dense plasma. Moscow Energoizdat 1986 (in Russian).
4. I.I.Sobelman. Introduction in Atomic Spectra Theory . Moscow, Nauka, 1963, p.640.(in Russian)
5. L.A.Vainstain, I.I.Sobelman, E.A.Yukov. Excitation of Atoms and Line Splitting. Moscow, Nauka, 1979, p.320. (in Russian)
6. G.A. Korn, T.M. Korn, Mathematical Handbook for Scientists and Engineers, McGraw-Hill Book Company, New York (1968).
7. Bazylev B.N., Kozlov I.M., Kozlova J.L., Romanov G.S. Numerical simulation of high temperature radiation waves. Matematicheskoe modelirovanie (in Russian) v.4, Nb 12, p. 23, 1992.
8. Zel'dovich Ya.B., Raizer Yu.P. Physics of Shock Waves and High-Temperature Hydrodynamic Phenomena. Academic Press. v. 1, 1966. 464p.
9. A.A. Samarsky, Theorie der Differenzverfahren, Akad. Verlagsgesellschaft Geestland porter Leipzig (1984).

Table 1

Calculated radiation heat fluxes to the wall and back radiated
for typical temperature and density profiles
of a beryllium plasma shield

	Radiative heat flux to wall	Back radiated flux
	MW/cm ²	
Multigroup Planck	0.23	7.2
Multigroup Rosseland	0.21	3.0
Two-level model for He- and H-like ions	0.30	8.0

Appendix 1. Asymptotic behavior of the difference schemes in the limit of optically thick plasma.

The radiation flux for an optically thick plasma has to be proportional to $-dB/d\tau$ where B is the Planck function and τ the optical thickness. (eq. 24). Eq. (24) can be written in a difference form by two ways depending on whether the source terms are defined in the center of meshes (half-integer index j) or whether they are defined at the mesh boundaries (integer index j):

$$S_{\varepsilon,j+1} = -A \left(\frac{B_{\varepsilon,j+3/2} - B_{\varepsilon,j+1/2}}{\Delta\tau_{\varepsilon,j+1}} \right) \quad (\text{A.1})$$

$$S_{\varepsilon,j+1} = -A \left(\frac{B_{\varepsilon,j+2} - B_{\varepsilon,j}}{\Delta\tau_{\varepsilon,j+1}} \right) \quad (\text{A.2})$$

$$A = 4\pi g^2$$

Here the Eddington factor g is the $\cos\mu$ averaged on the total solid angle. Therefore in the limit of the optically thick plasma all the difference schemes with source terms defined in mesh centers have to be transformed into equations like (A.1) and difference schemes with source terms defined in the mesh boundaries have to be transformed into equations like (A.2).

The asymptotic behavior of the difference schemes of eqs. (17), (18), (19) are investigated below for the case of an optically thick plasma. The following assumptions are used: $\Delta\tau = \kappa\Delta l \rightarrow \infty$, the LTE assumption is fulfilled and the radiation intensity becomes close to the blackbody radiation, equidistant meshes are used with a view to simplification.

The difference scheme (17) with source terms and absorption coefficients defined at the mesh boundaries in case of optically thick plasma is transformed into the following form:

$$\begin{aligned} I_{\varepsilon,j+1,i} &= \frac{\Delta l_{j+1/2,i} (J_{\varepsilon})_{j+1,i} + I_{\varepsilon,j,i}}{\kappa_{\varepsilon,j+1} \Delta l_{j+1/2,i}}, \quad \mu_i > 0 \\ I_{\varepsilon,j+1,i} &= \frac{\Delta l_{j+3/2,i} (J_{\varepsilon})_{j+1,i} + I_{\varepsilon,j+2,i}}{\kappa_{\varepsilon,j+1} \Delta l_{j+3/2,i}}, \quad \mu_i < 0 \end{aligned} \quad (\text{A.3})$$

In the LTE assumption the source is given as product of the Planck function and the absorption coefficient. Thus eqs. (A.3) can be rewritten according to:

$$\begin{aligned}
I^+ &= I_{\varepsilon,j+1,i} = (B_\varepsilon)_{j+1,i} + \frac{I_{\varepsilon,j,i}}{\Delta\tau_{j+1,i}}, \quad \mu_i > 0 \\
I^- &= I_{\varepsilon,j+1,i} = (B_\varepsilon)_{j+1,i} + \frac{I_{\varepsilon,j+2,i}}{\Delta\tau_{j+1,i}}, \quad \mu_i < 0
\end{aligned} \tag{A.4}$$

Subtracting the second equation from the first one the analog of the radiative flux is obtained for the given angle μ_i :

$$\begin{aligned}
(I^+ - I^-)_{\varepsilon,j+1,i} &= \frac{I_{\varepsilon,j,i}}{\Delta\tau_{j+1,i}} - \frac{I_{\varepsilon,j+2,i}}{\Delta\tau_{j+1,i}} = -\frac{I_{\varepsilon,j+2,i} - I_{\varepsilon,j,i}}{\Delta\tau_{j+1,i}} \\
&\cong -\frac{B_{\varepsilon,j+2,i} - B_{\varepsilon,j,i}}{\Delta\tau_{j+1,i}}
\end{aligned} \tag{A.5}$$

To get the radiative flux eq. (A.5) has to be integrated with weight μ over the half of the solid angle. After integration the analog of equation (A.2) is obtained. Therefore the difference scheme (17) has the correct asymptotic behavior of the radiative flux for an optically thick plasma.

If the source terms and the absorption coefficients are defined in the center of the meshes the following expressions can be written:

$$\begin{aligned}
I_{\varepsilon,j+1,i} &= \frac{\Delta l_{j+1/2,i} (J_\varepsilon)_{j+1/2,i} + I_{\varepsilon,j,i}}{\kappa_{\varepsilon,j+1/2} \Delta l_{j+1/2,i}}, \quad \mu_i > 0 \\
I_{\varepsilon,j+1,i} &= \frac{\Delta l_{j+3/2,i} (J_\varepsilon)_{j+3/2,i} + I_{\varepsilon,j+2,i}}{\kappa_{\varepsilon,j+3/2} \Delta l_{j+3/2,i}}, \quad \mu_i < 0
\end{aligned} \tag{A.6}$$

For an optically thick plasma eqs. (A.6) can be rewritten according to:

$$\begin{aligned}
I^+ &= I_{\varepsilon,j+1,i} = (B_\varepsilon)_{j+1/2,i} + \frac{I_{\varepsilon,j,i}}{\Delta\tau_{j+1/2,i}}, \quad \mu_i > 0 \\
I^- &= I_{\varepsilon,j+1,i} = (B_\varepsilon)_{j+3/2,i} + \frac{I_{\varepsilon,j+2,i}}{\Delta\tau_{j+3/2,i}}, \quad \mu_i < 0
\end{aligned} \tag{A.7}$$

Subtracting the second equation from the first one the analog of the radiative flux is obtained for the given angle μ_i :

$$\begin{aligned}
(I^+ - I^-)_{\varepsilon, j+1, i} &= B_{\varepsilon, j+1/2} - B_{\varepsilon, j+3/2} + \frac{I_{\varepsilon, j, i}}{\Delta\tau_{j+1/2, i}} - \frac{I_{\varepsilon, j+2, i}}{\Delta\tau_{j+3/2, i}} = \\
&= -(B_{\varepsilon, j+3/2} - B_{\varepsilon, j+1/2}) - \left(\frac{B_{\varepsilon, j+2, i}}{\Delta\tau_{j+3/2, i}} - \frac{B_{\varepsilon, j, i}}{\Delta\tau_{j+1/2, i}} \right)
\end{aligned} \tag{A.8}$$

The term in the second brackets has the form being close to the derivative of the Planck function on the optical thickness (the correct asymptotic behavior (see eq. (A.2)). But the term in the first bracket is the simple difference between the Planckian functions in the neighboring meshes. This term dominates for all the cases $\Delta\tau \geq 1$. Therefore in the case of rather large temperature gradient the radiative flux calculated using difference schemes of such kind is significantly overestimated if $\Delta\tau \geq 1$. Error of the radiation flux calculations is proportional to the optical thickness of the meshes and rises with increasing the optical thickness of a mesh and roughing the mesh grid.

The difference schemes (18) and (19) are investigated by the same way. For simplification of the difference scheme analysis $\exp(-k\Delta l)$ is expanded into Taylor series up to first term and is used in the following form:

$$\exp(-k\Delta l) \approx \frac{1}{1 + k\Delta l} \tag{A.9}$$

Thus in case of an optically thick plasma ($\Delta\tau = \kappa\Delta l \rightarrow \infty$) the terms containing $\exp(-k\Delta l)$ in expressions (18), (19) have the following limits:

$$\begin{aligned}
1 - \exp(-k\Delta l) &\approx 1 - \frac{1}{1 + k\Delta l} = \frac{1 + k\Delta l - 1}{1 + k\Delta l} = \frac{k\Delta l}{1 + k\Delta l} \rightarrow_{\tau \rightarrow \infty} \mathbf{1} \\
1 - \frac{1 - \exp(-k\Delta l)}{k\Delta l} &\approx 1 - \frac{\frac{k\Delta l}{1 + k\Delta l}}{k\Delta l} = 1 - \frac{k\Delta l}{k\Delta l + (k\Delta l)^2} \rightarrow_{\tau \rightarrow \infty} \mathbf{1} \\
\frac{1 - \exp(-k\Delta l)}{k\Delta l} - \exp(-k\Delta l) &\approx \frac{k\Delta l}{k\Delta l + (k\Delta l)^2} - \frac{1}{1 + k\Delta l} \approx \\
&\approx \frac{k\Delta l}{k\Delta l + (k\Delta l)^2} - \frac{1}{k\Delta l} \rightarrow_{\tau \rightarrow \infty} \mathbf{0}
\end{aligned} \tag{A.10}$$

Using the limits (A.9) and (A.10) the integral difference scheme with source terms defined in the mesh centers (eq. 18) can be rewritten by the following way:

$$I^+ = I_{\varepsilon,j+1,i} = I_{\varepsilon,j,i} \frac{1}{1+k_{\varepsilon,j+1/2}\Delta l} + \frac{1}{\kappa_{\varepsilon,j+1/2}} J_{\varepsilon,j+1/2} \frac{k_{\varepsilon,j+1/2}\Delta l}{1+k_{\varepsilon,j+1/2}\Delta l}, \quad \mu_i > 0 \quad (\text{A.11})$$

$$I^- = I_{\varepsilon,j+1,i} = I_{\varepsilon,j+2,i} \frac{1}{1+k_{\varepsilon,j+3/2}\Delta l} + \frac{1}{\kappa_{\varepsilon,j+3/2}} J_{\varepsilon,j+3/2} \frac{k_{\varepsilon,j+3/2}\Delta l}{1+k_{\varepsilon,j+3/2}\Delta l}, \quad \mu_i < 0$$

Subtracting the second equation from the first one in the limit of $\tau \rightarrow \infty$ the expression analogous to eq. (A.8) is obtained.

$$\begin{aligned} (I^+ - I^-)_{\varepsilon,j+1,i} &= B_{\varepsilon,j+1/2} - B_{\varepsilon,j+3/2} + \frac{I_{\varepsilon,j,i}}{\Delta\tau_{j+1/2,i}} - \frac{I_{\varepsilon,j+2,i}}{\Delta\tau_{j+3/2,i}} = \\ &= -(B_{\varepsilon,j+3/2} - B_{\varepsilon,j+1/2}) - \left(\frac{B_{\varepsilon,j+2,i}}{\Delta\tau_{j+3/2,i}} - \frac{B_{\varepsilon,j,i}}{\Delta\tau_{j+1/2,i}} \right) \end{aligned} \quad (\text{A.12})$$

Thus the integral difference scheme with source terms defined in the mesh centers also has no correct limit in case of an optically thick plasma. Difference schemes of such kind can be used for the radiation transfer calculations if condition $\Delta\tau < 1$ is satisfied for all the meshes and frequency groups.

The integral difference scheme (19) with source terms defined in the mesh boundaries can be rewritten in analogy to (A.11) in the following form:

$$\begin{aligned} I^+ &= I_{\varepsilon,j+1,i} = I_{\varepsilon,j,i} \frac{1}{1+k_{\varepsilon,j+1}\Delta l} + \frac{1}{\kappa_{\varepsilon,j+1}} J_{\varepsilon,j+1} \left(1 - \frac{k_{\varepsilon,j+1/2}\Delta l}{k_{\varepsilon,j+1/2}\Delta l + (k_{\varepsilon,j+1/2}\Delta l)^2} \right) + \\ &+ \frac{1}{\kappa_{\varepsilon,j}} J_{\varepsilon,j} \left(\frac{k_{\varepsilon,j+1/2}\Delta l}{k_{\varepsilon,j+1/2}\Delta l + (k_{\varepsilon,j+1/2}\Delta l)^2} - \frac{1}{1+k_{\varepsilon,j+1/2}\Delta l} \right), \quad \mu_i > 0 \\ I^- &= I_{\varepsilon,j+1,i} = I_{\varepsilon,j+2,i} \frac{1}{1+k_{\varepsilon,j+1}\Delta l} + \frac{1}{\kappa_{\varepsilon,j+1}} J_{\varepsilon,j+1} \left(1 - \frac{k_{\varepsilon,j+3/2}\Delta l}{k_{\varepsilon,j+3/2}\Delta l + (k_{\varepsilon,j+3/2}\Delta l)^2} \right) + \\ &+ \frac{1}{\kappa_{\varepsilon,j}} J_{\varepsilon,j+2} \left(\frac{k_{\varepsilon,j+3/2}\Delta l}{k_{\varepsilon,j+3/2}\Delta l + (k_{\varepsilon,j+3/2}\Delta l)^2} - \frac{1}{1+k_{\varepsilon,j+3/2}\Delta l} \right), \quad \mu_i < 0 \end{aligned} \quad (\text{A.13})$$

Using the limits (A.9) and (A.10) in the limit $\tau \rightarrow \infty$ the eq. (A.13) can be rewritten by the following way:

$$\begin{aligned} I^+ &= I_{\varepsilon,j+1,i} = I_{\varepsilon,j} \frac{1}{\tau_{\varepsilon,j+1}} + B_{\varepsilon,j+1}, \quad \mu_i > 0 \\ I^- &= I_{\varepsilon,j+1,i} = I_{\varepsilon,j+2} \frac{1}{\tau_{\varepsilon,j+1}} + B_{\varepsilon,j+1}, \quad \mu_i < 0 \end{aligned} \quad (\text{A.14})$$

Subtracting the second equation from the first one the analog of the radiative flux is obtained for the given angle μ_i :

$$\begin{aligned}
 (I^+ - I^-)_{\varepsilon, j+1, i} &= \frac{I_{\varepsilon, j, i}}{\Delta\tau_{j+1, i}} - \frac{I_{\varepsilon, j+2, i}}{\Delta\tau_{j+1, i}} = -\frac{I_{\varepsilon, j+2, i} - I_{\varepsilon, j, i}}{\Delta\tau_{j+1, i}} \\
 &\cong -\frac{B_{\varepsilon, j+2, i} - B_{\varepsilon, j, i}}{\Delta\tau_{j+1, i}}
 \end{aligned}
 \tag{A.15}$$

Eq. (A.15) coincides with eq. (A.5). Therefore the integral difference scheme (19) has the correct limit in case of an optically thick plasma also.

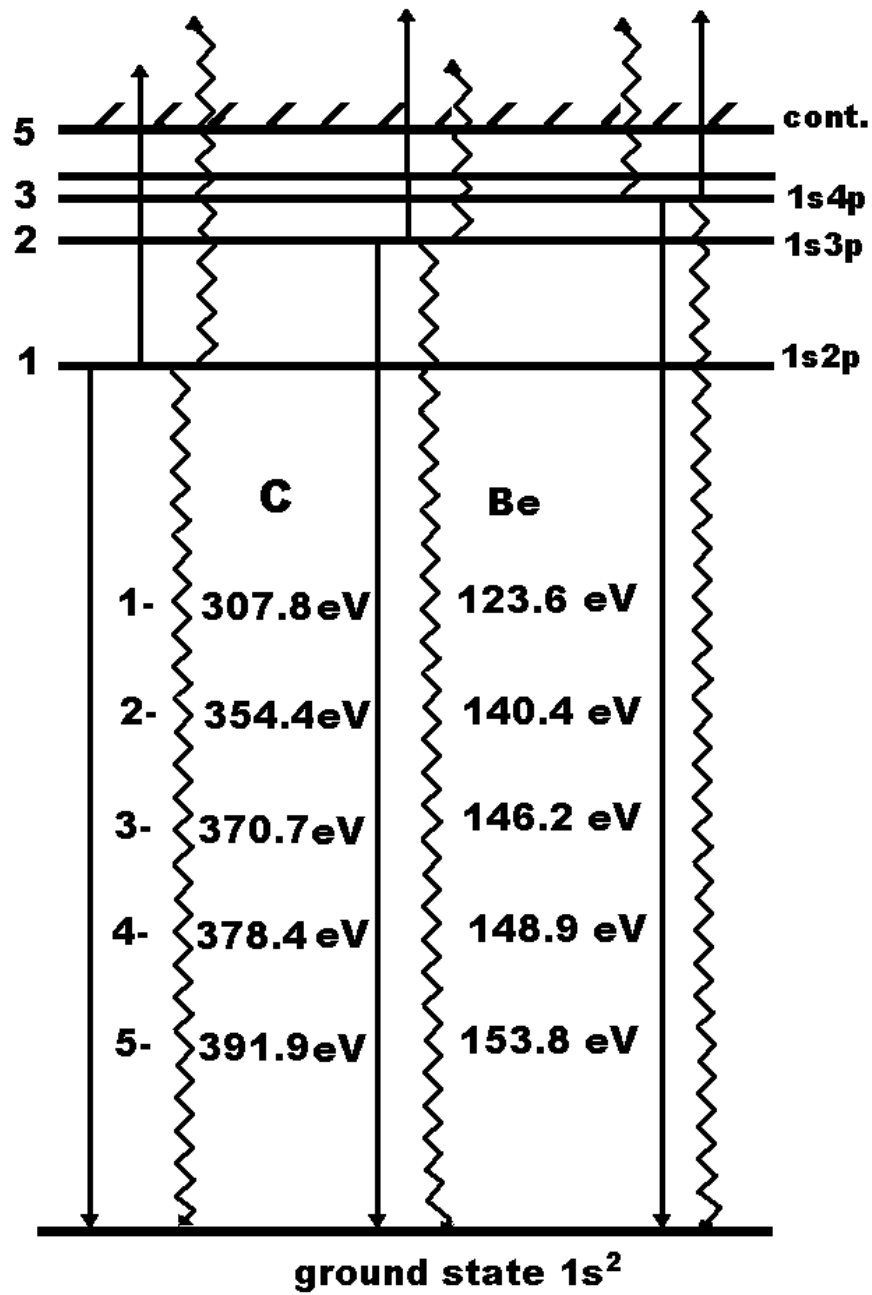


Fig. 1a. Energy level structure of the He-like ions of beryllium and carbon.

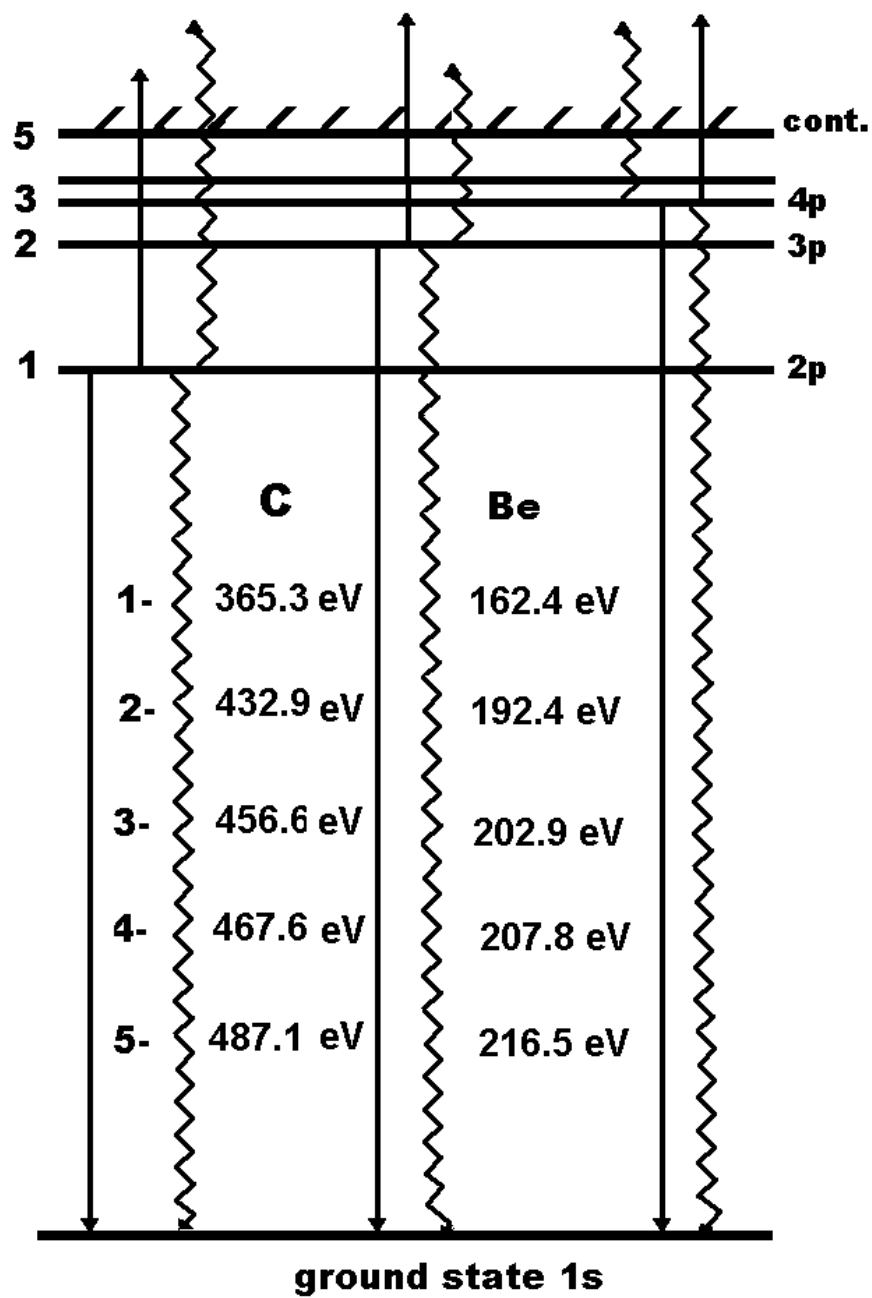


Fig. 1b. Energy level structure of the H-like ions of beryllium and carbon.

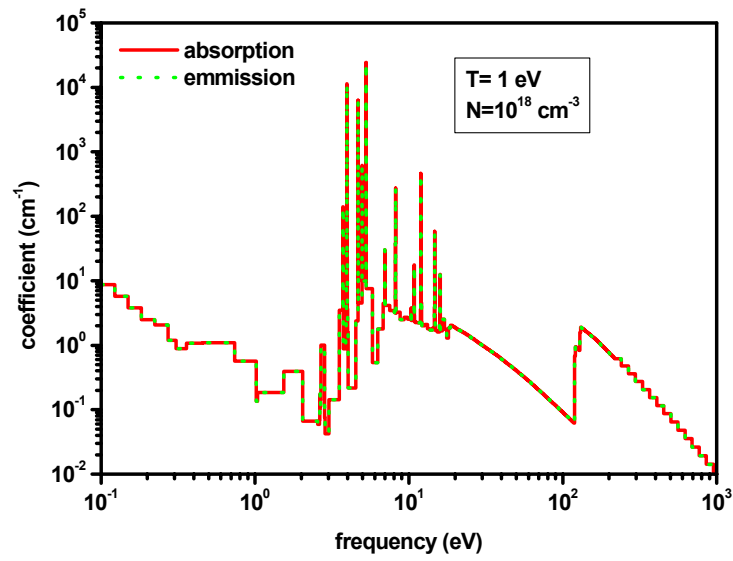


Fig. 2a. Absorption and emission coefficients of Be plasma at temperature $T=1$ eV and density $N=10^{18}$ cm^{-3} .

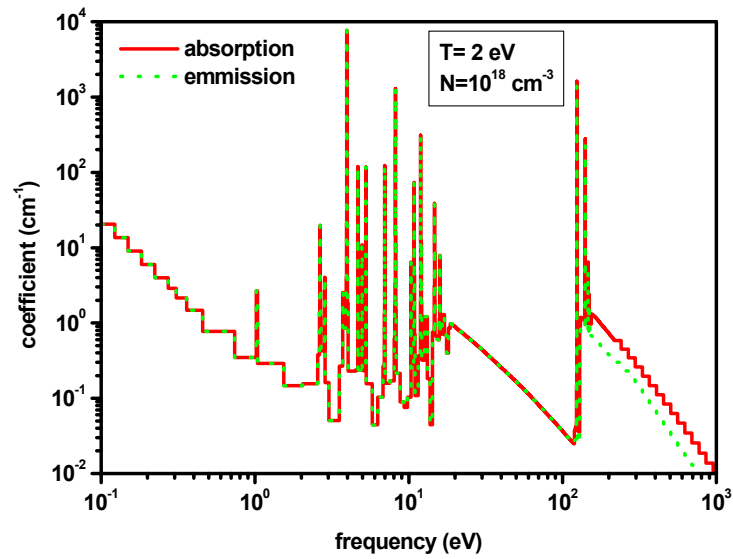


Fig. 2b. Absorption and emission coefficients of Be plasma at temperature $T=2$ eV and density $N=10^{18}$ cm^{-3} .

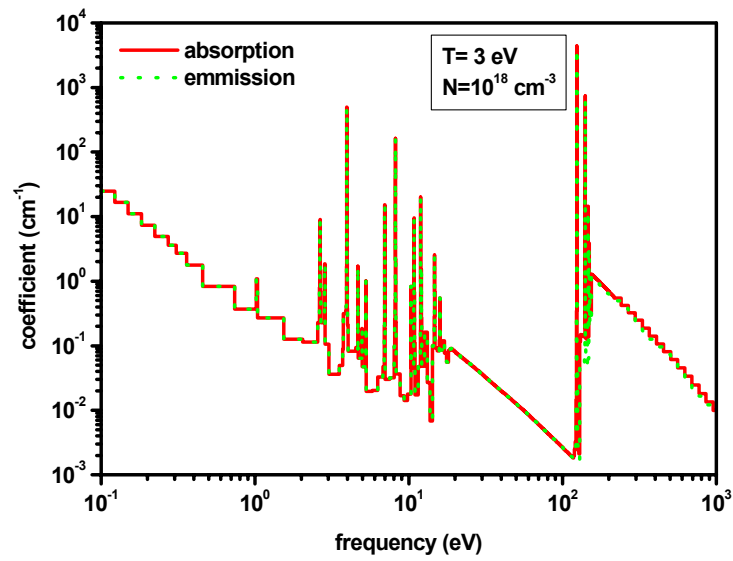


Fig. 2c. Absorption and emission coefficients of Be plasma at temperature $T=3$ eV and density $N=10^{18}$ cm^{-3} .

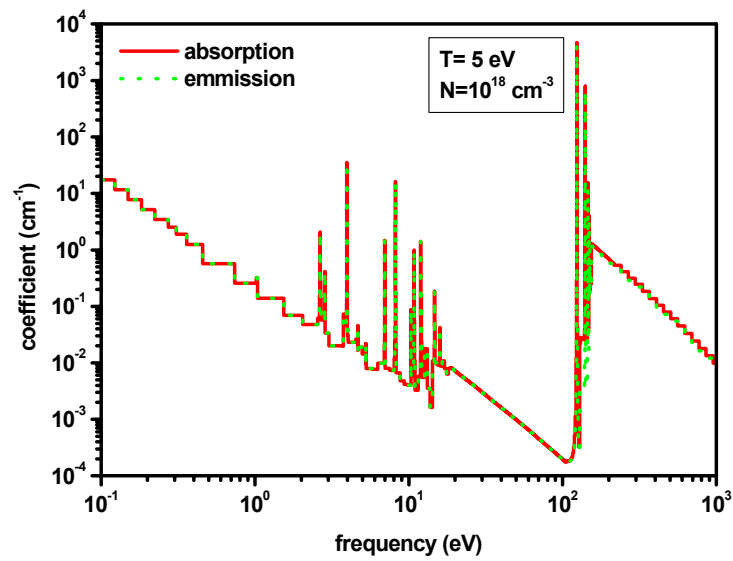


Fig. 2d. Absorption and emission coefficients of Be plasma at temperature $T=5$ eV and density $N=10^{18}$ cm^{-3} .

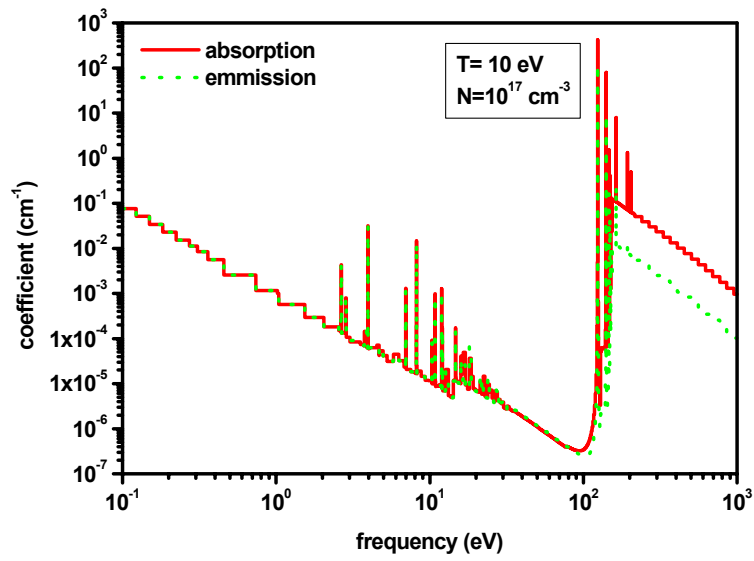


Fig. 2e. Absorption and emission coefficients of Be plasma at temperature $T=10$ eV and density $N=10^{17}$ cm^{-3} .

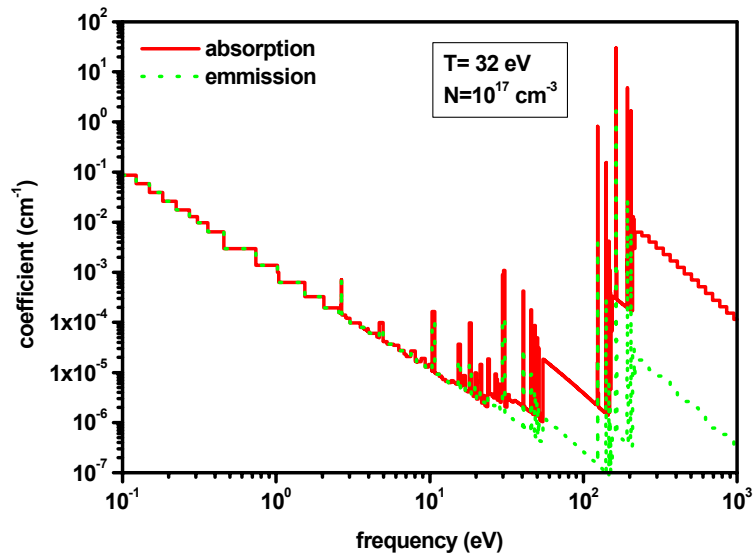


Fig. 2f. Absorption and emission coefficients of Be plasma at temperature $T=32$ eV and density $N=10^{17}$ cm^{-3} .

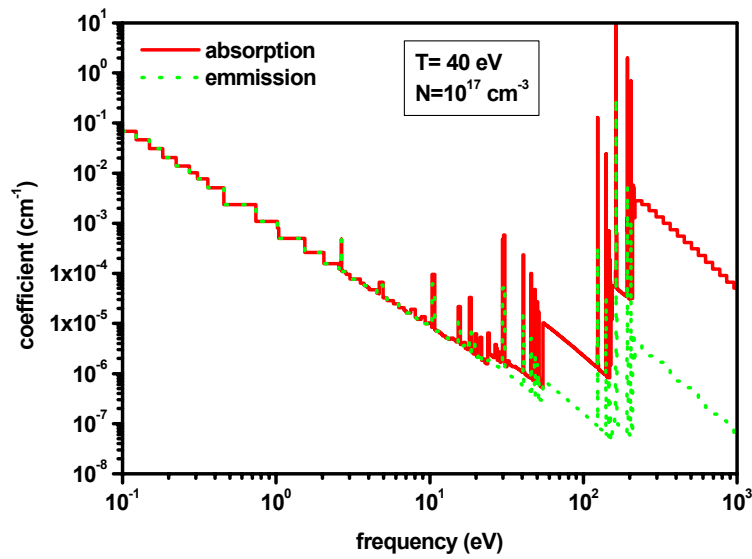


Fig. 2g. Absorption and emission coefficients of Be plasma at temperature $T=40$ eV and density $N=10^{17}$ cm^{-3} .

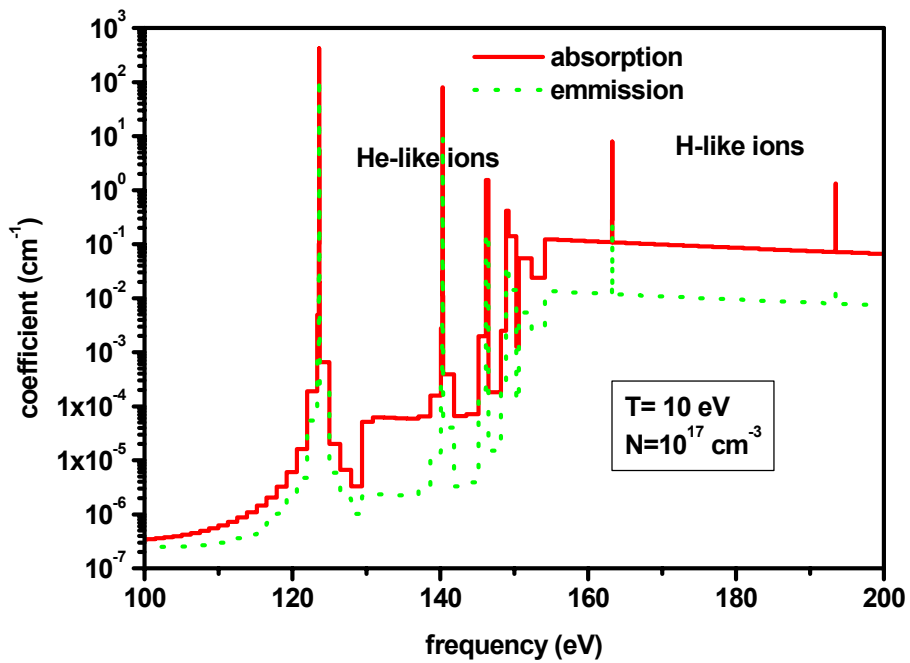


Fig. 3a. Absorption and emission coefficients of a Be plasma in the soft X-ray region showing the lines from He- and H- like ions at a plasma temperature of 10 eV and density of 10^{17} cm^{-3} .

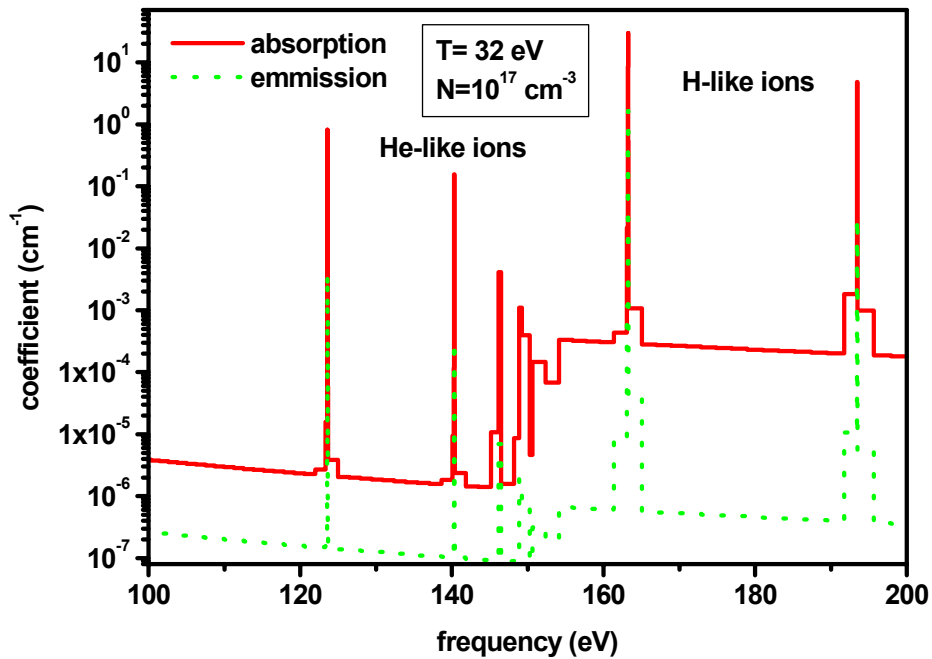


Fig. 3b. Absorption and emission coefficients of a Be plasma in the soft X-ray region showing the lines from He- and H- like ions at a plasma temperature of 32 eV and density of 10^{17} cm^{-3} .

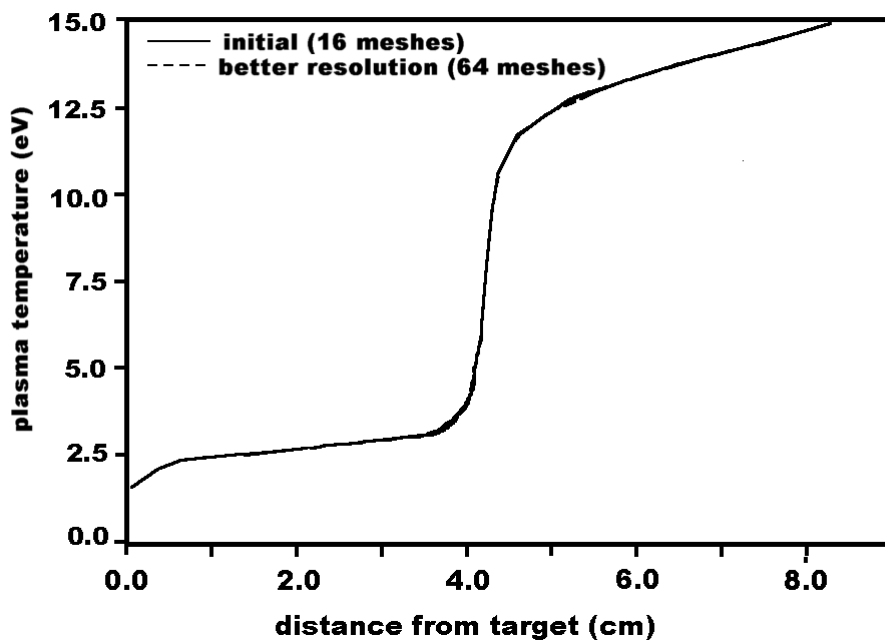


Fig. 4. Typical profile of plasma temperature in a beryllium plasma layer as used.

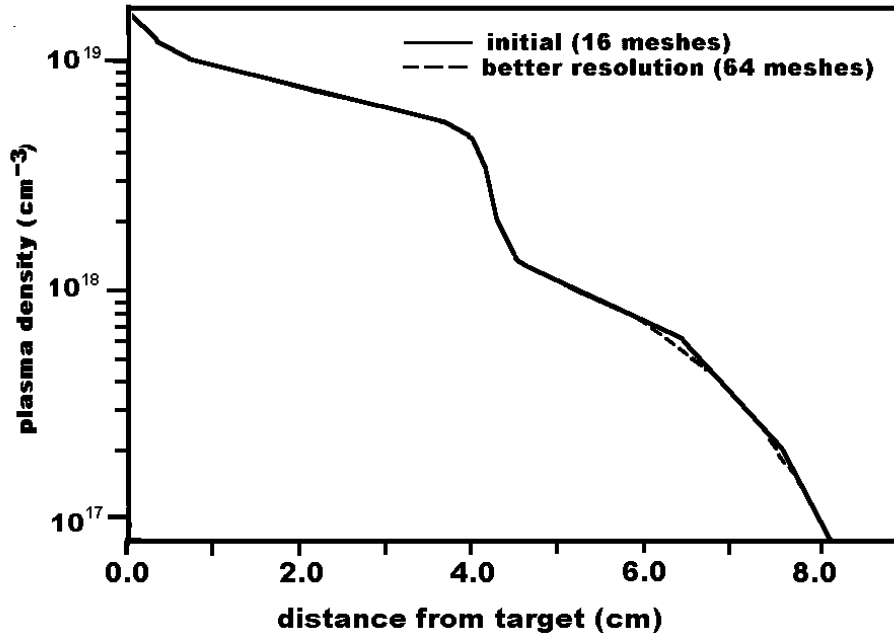


Fig. 5. Typical profile of plasma density in a beryllium plasma layer as used

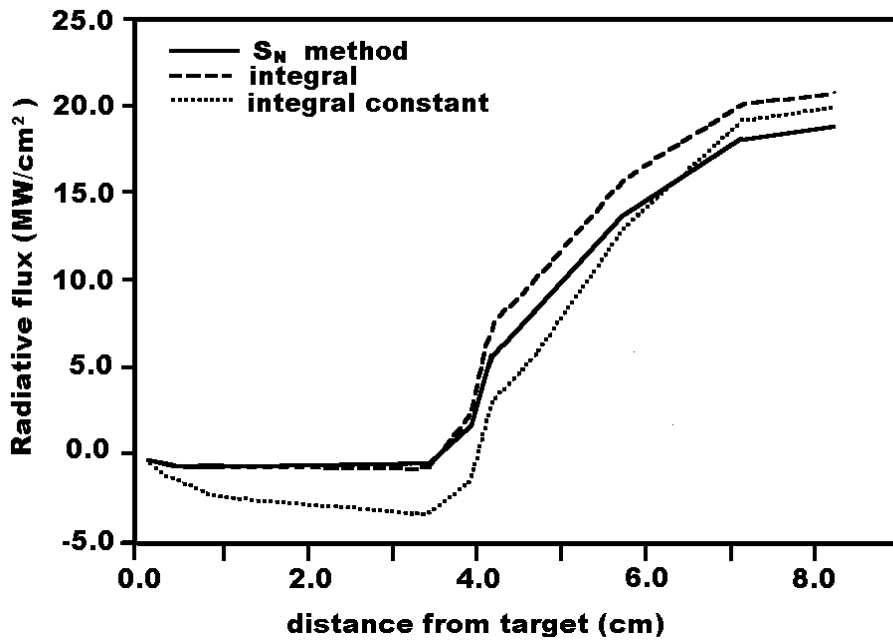


Fig. 6. Total radiation flux, calculated by different methods using the initial profile

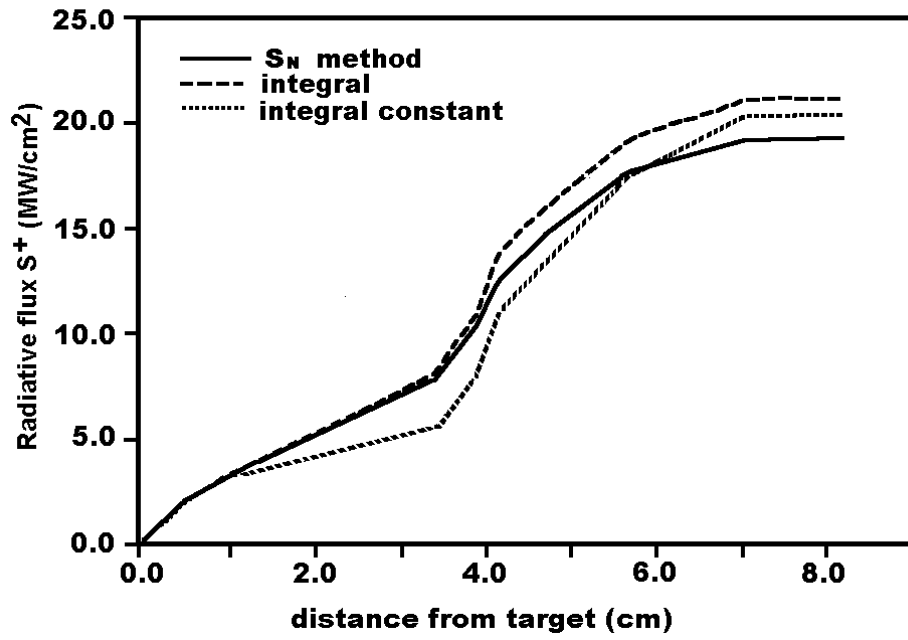


Fig. 7. Radiation flux in positive ($\mu > 0$) direction, calculated by different methods using the initial profile

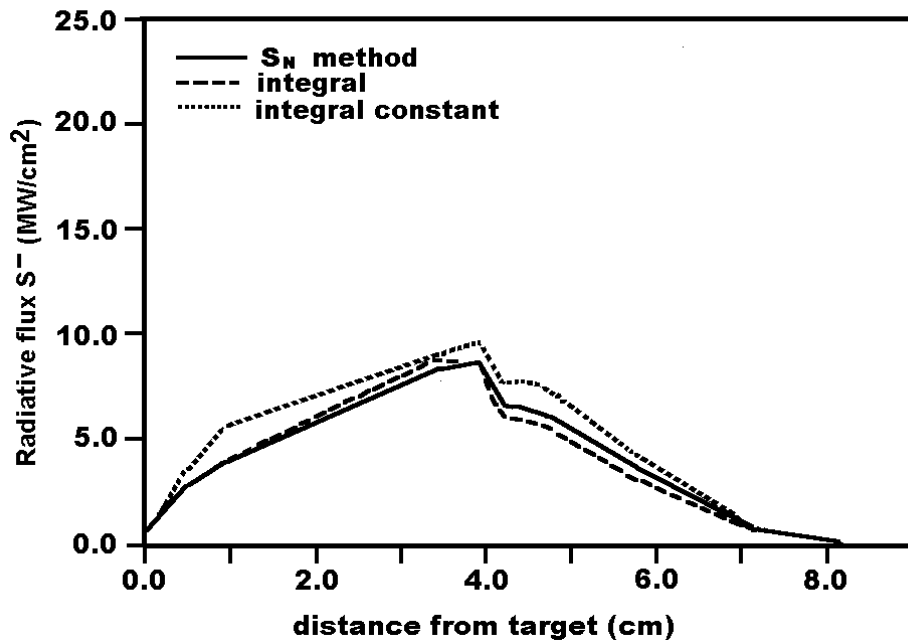


Fig. 8. Radiation flux in negative ($\mu < 0$) direction, calculated by different methods using the initial profile

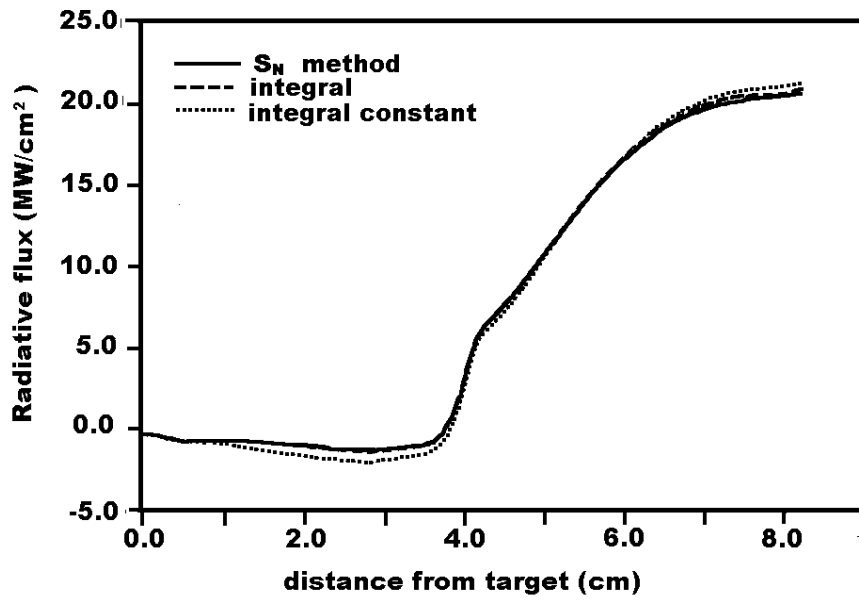


Fig. 9. Total radiation flux, calculated by different methods using the adequately resolved profile

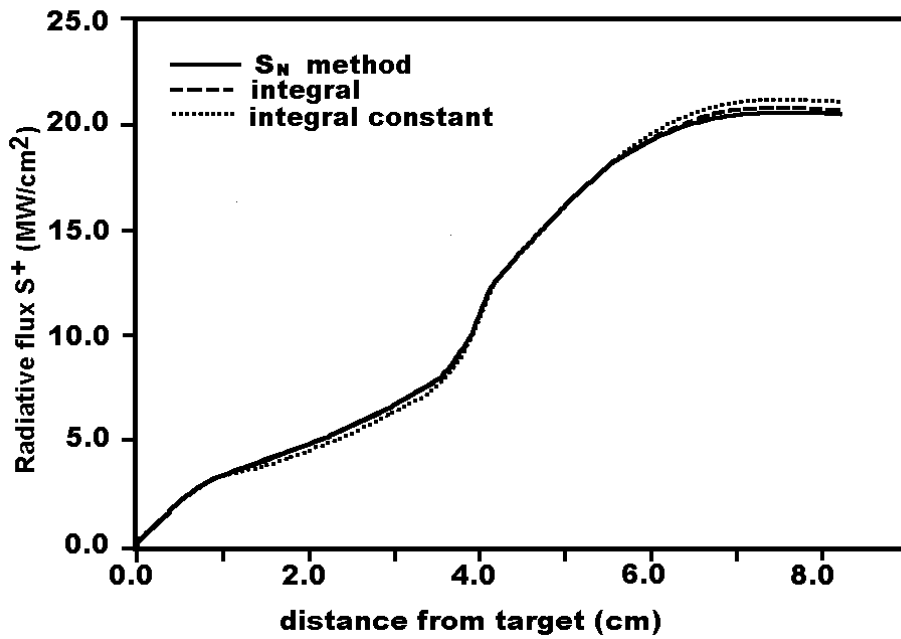


Fig. 10. Radiation flux in positive ($\mu > 0$) direction, calculated by different methods using the adequately resolved profile

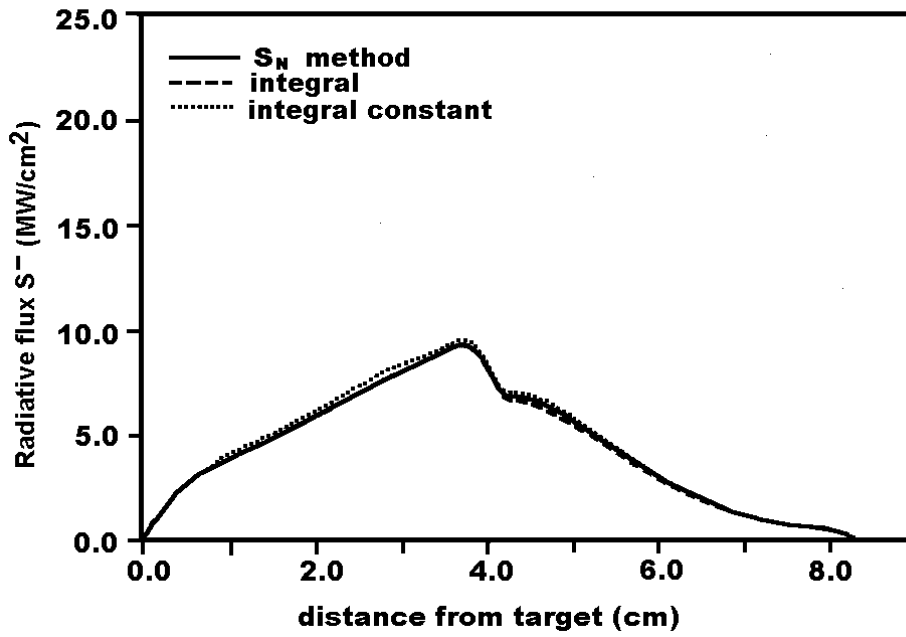


Fig. 11. Radiation flux in negative ($\mu < 0$) direction, calculated by different methods using the adequately resolved profile

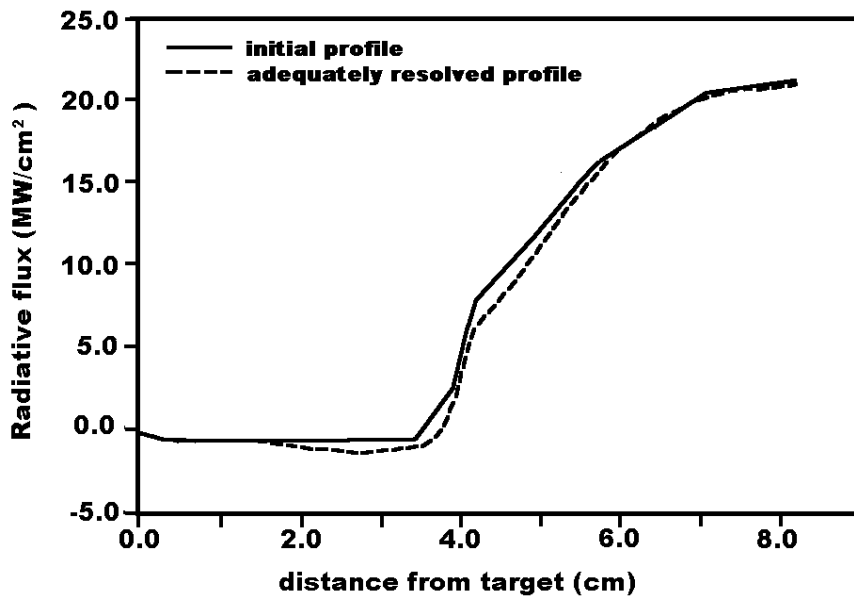


Fig. 12. Comparison of total radiation fluxes calculated with different mesh resolution using the linear integral method

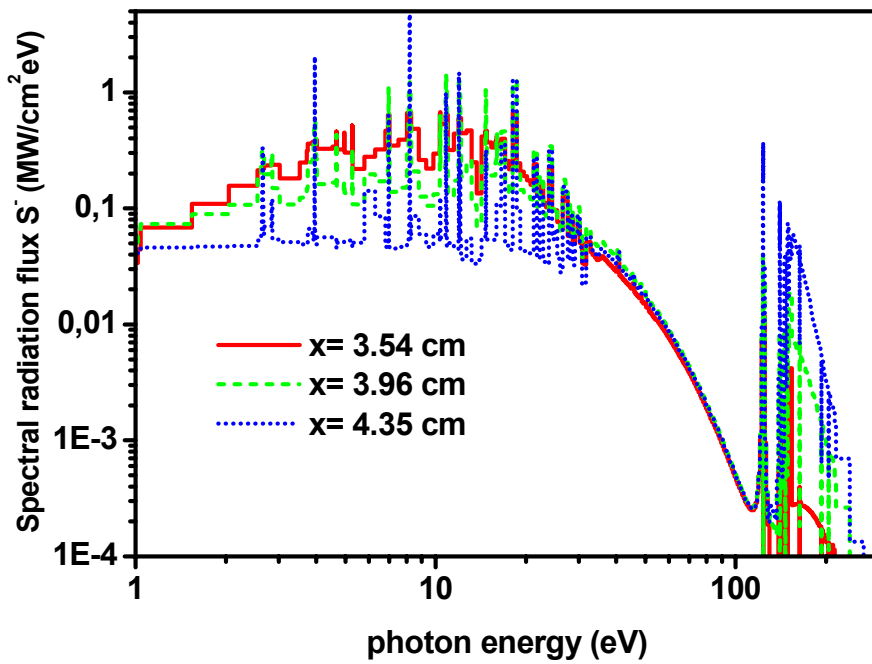


Fig. 13. Typical spectral radiation flux in negative ($\mu < 0$) direction at different positions in the vicinity of the transition region.

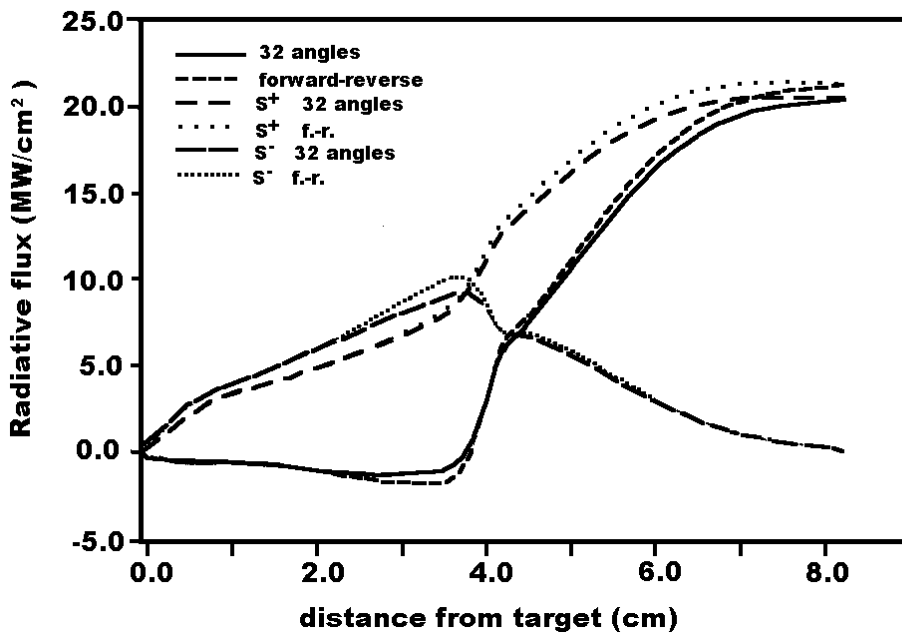


Fig. 14. Comparison calculated radiative fluxes using the forward-reverse method and the S_N method with high angle resolution (fixed profile with 64 meshes).

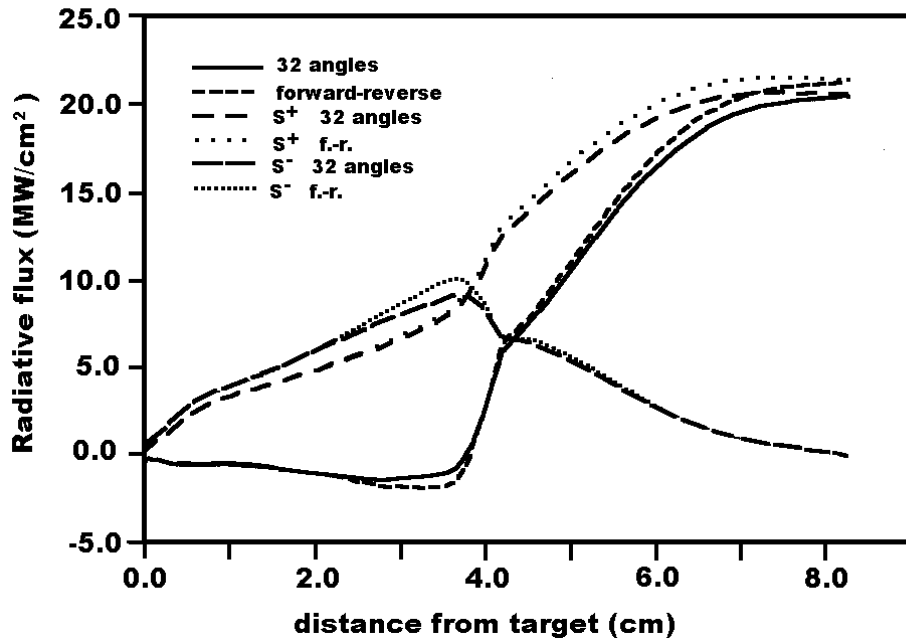


Fig. 15. Comparison calculated radiative fluxes using the forward-reverse method and the constant integral method with high angle resolution (fixed profile with 64 meshes).

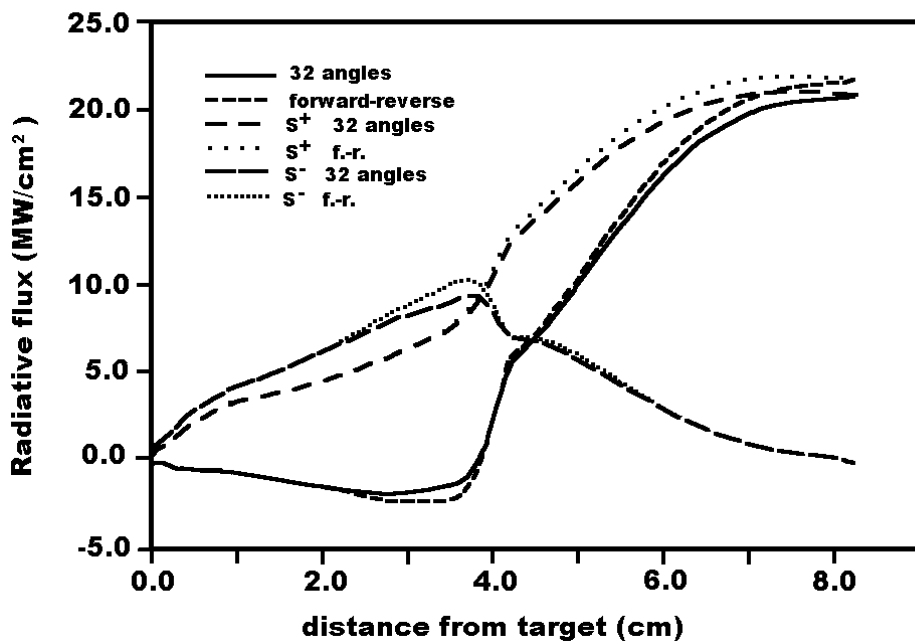


Fig. 16. Comparison calculated radiative fluxes using the forward-reverse method and the linear integral method with high angle resolution (fixed profile with 64 meshes).

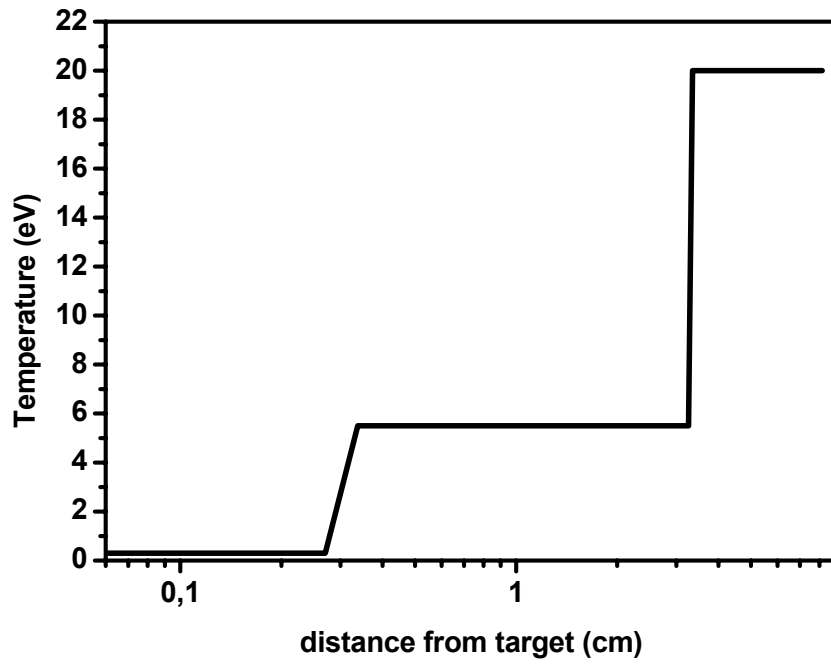


Fig. 17. Temperature profile for first test variant

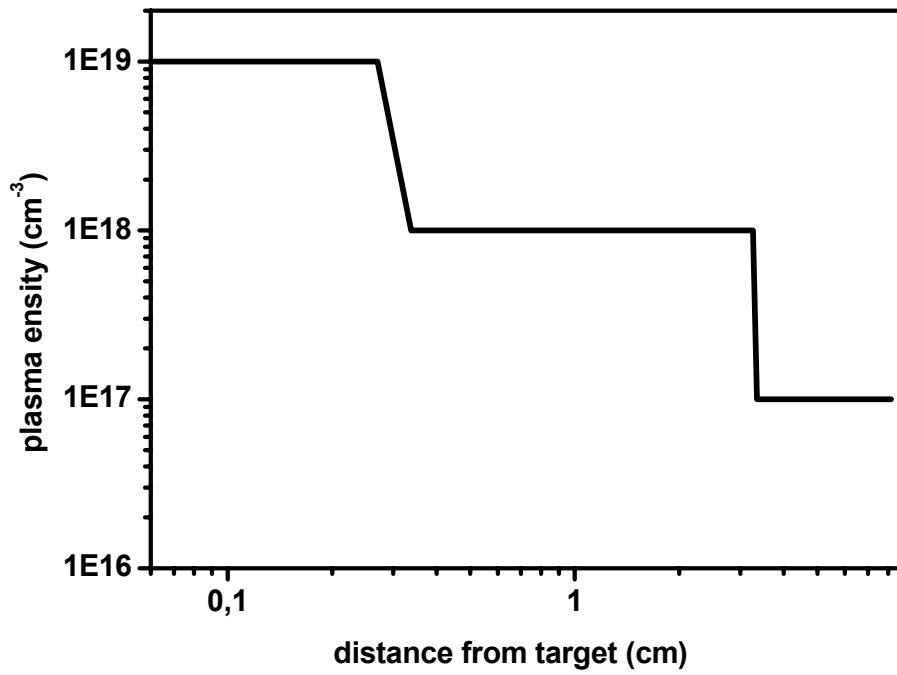


Fig. 18. Density profile for first test variant

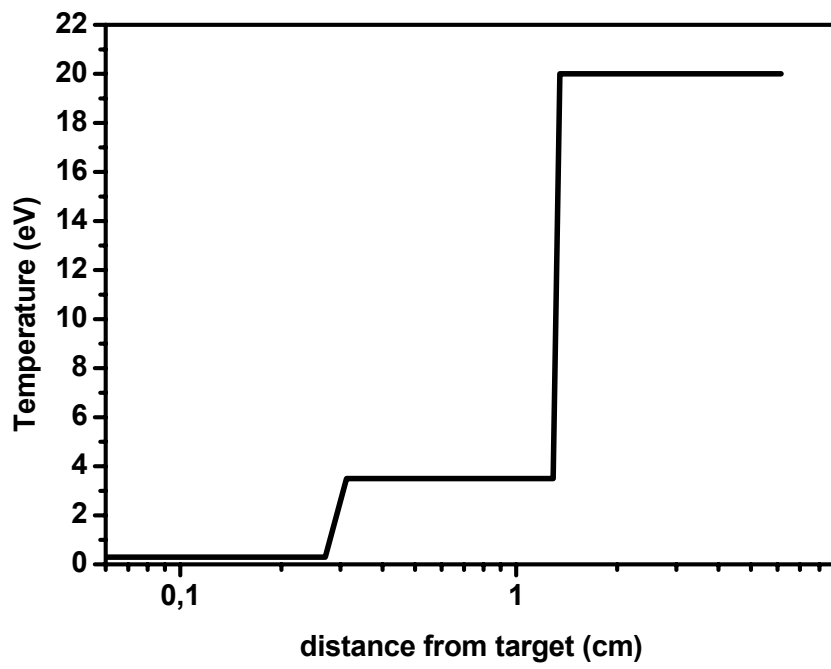


Fig. 19. Temperature profile for second test variant

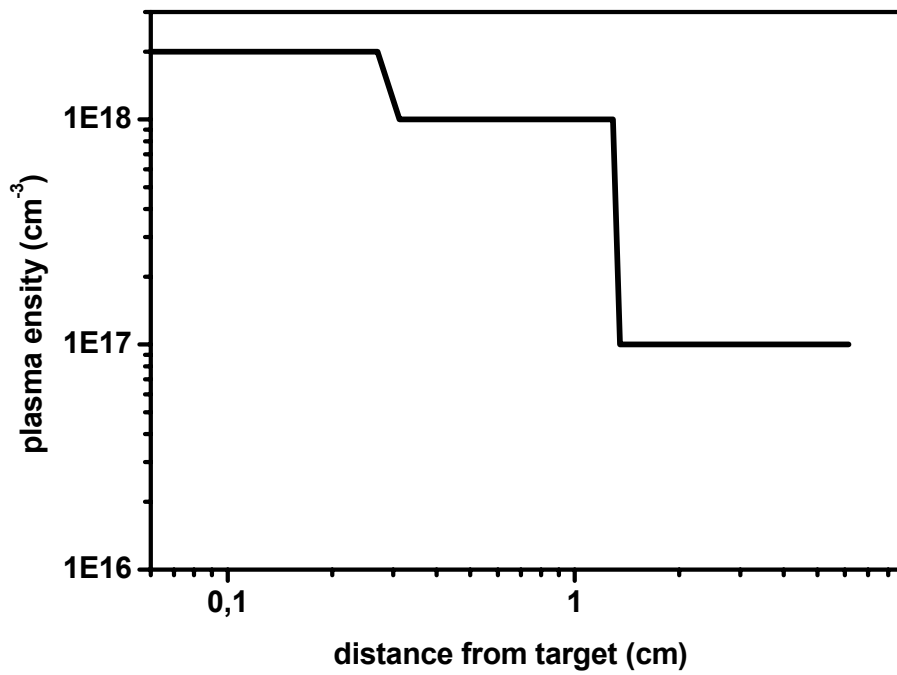


Fig. 20. Density profile for second test variant

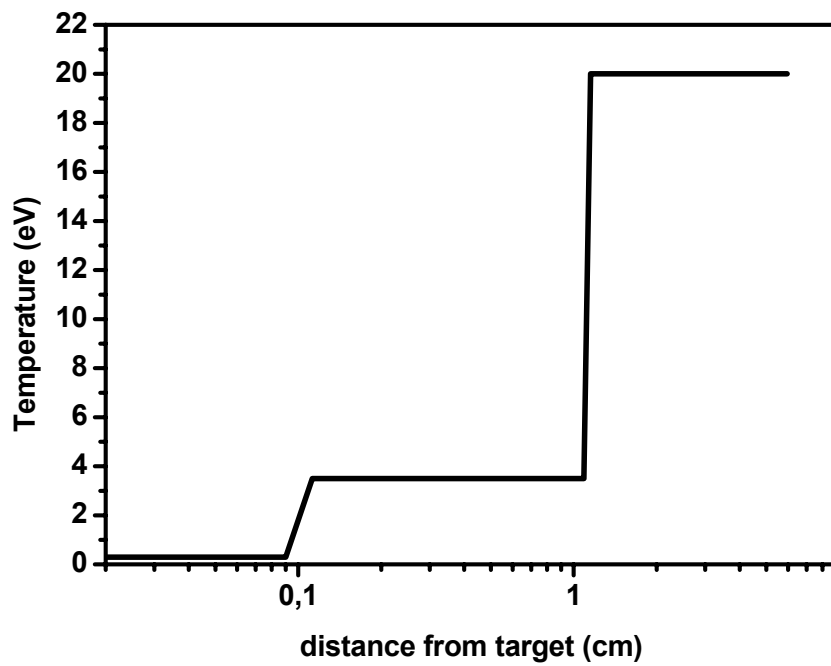


Fig. 21. Temperature profile for third test variant.

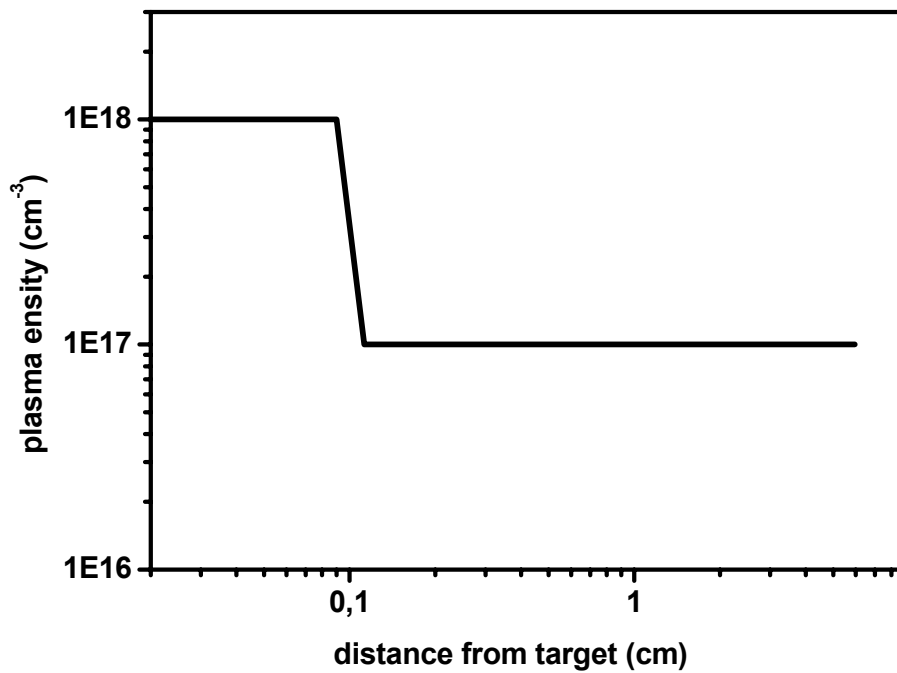


Fig. 22. Density profile for third test variant.

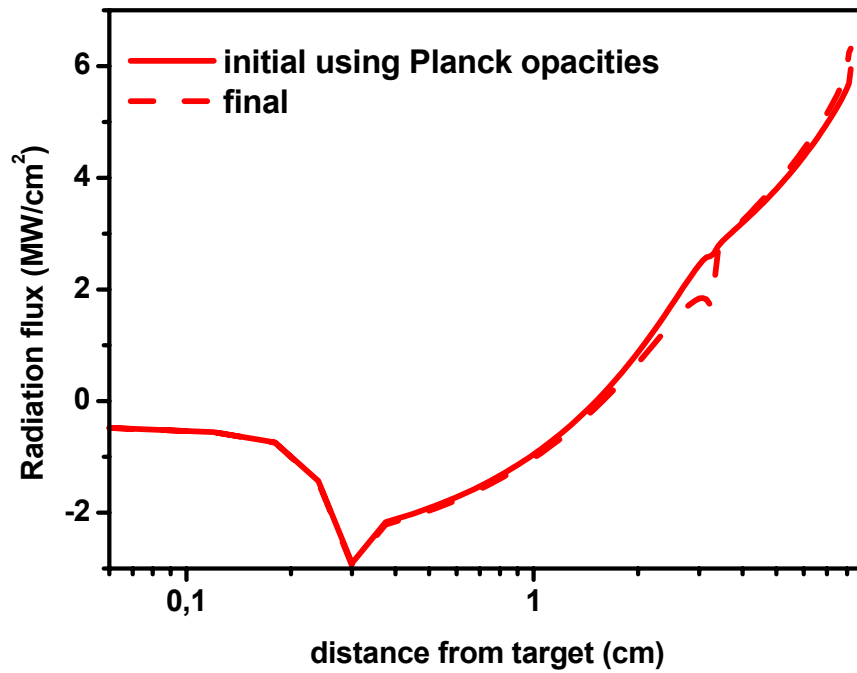


Fig. 23. Total radiation flux calculated for the first test variant (initial and final after 15 iterations) by use of the two level model and the linear integral transport method.

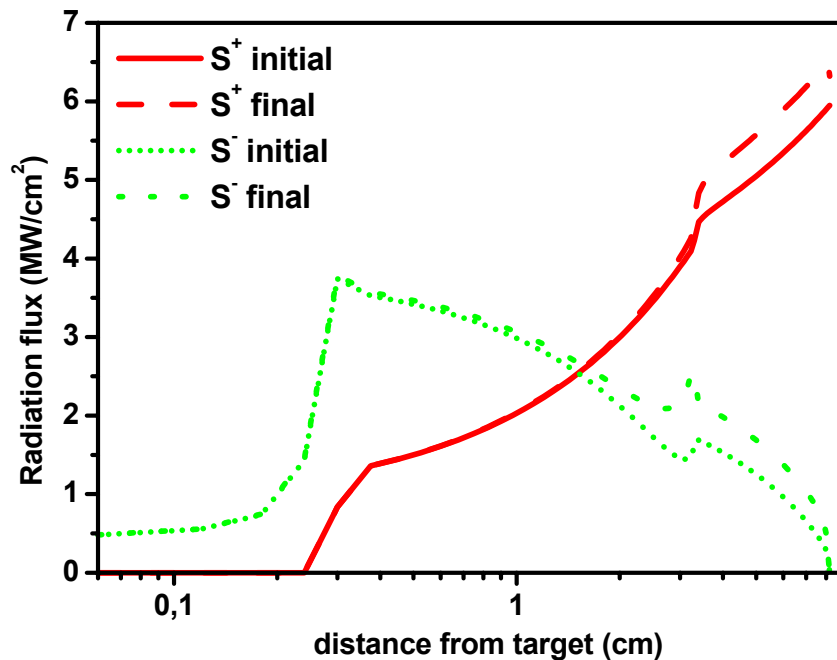


Fig. 24. Radiation flux in positive ($\mu > 0$) and negative ($\mu < 0$) directions for the first test variant (initial and final after 15 iterations) by use of the two level model and the linear integral transport method.

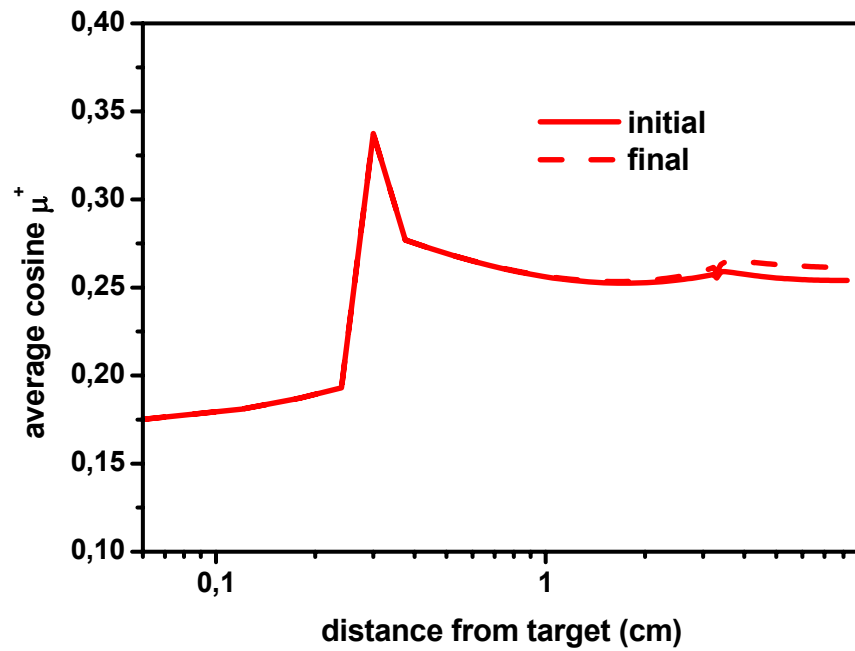


Fig. 25. Average cosine in positive direction ($\mu > 0$) for the first test variant (initial and final after 15 iterations) by use of the two level model and the linear integral transport method.

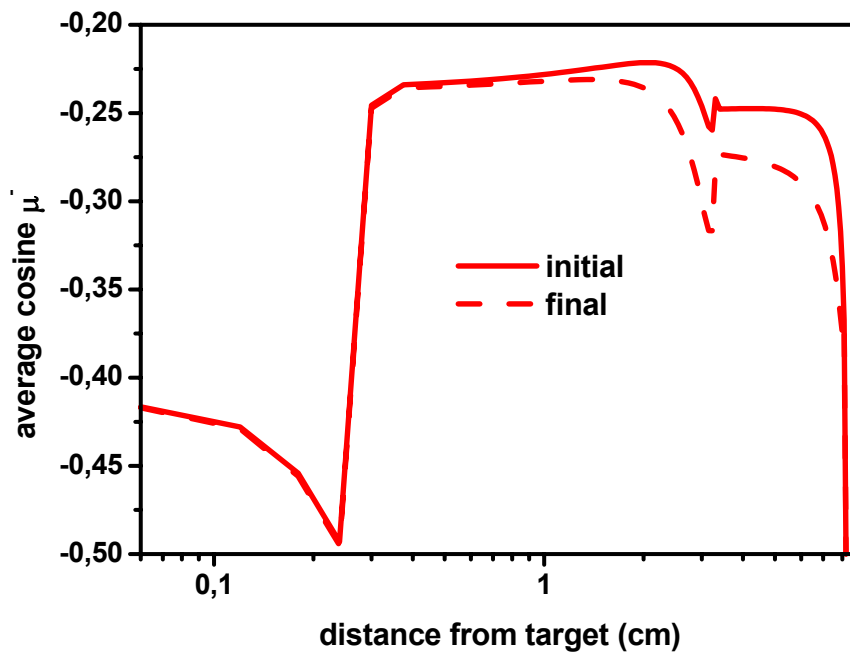


Fig. 26. Average cosine in negative direction ($\mu < 0$) for the first test variant (initial and final after 15 iterations) by use of the two level model and the linear integral transport method.

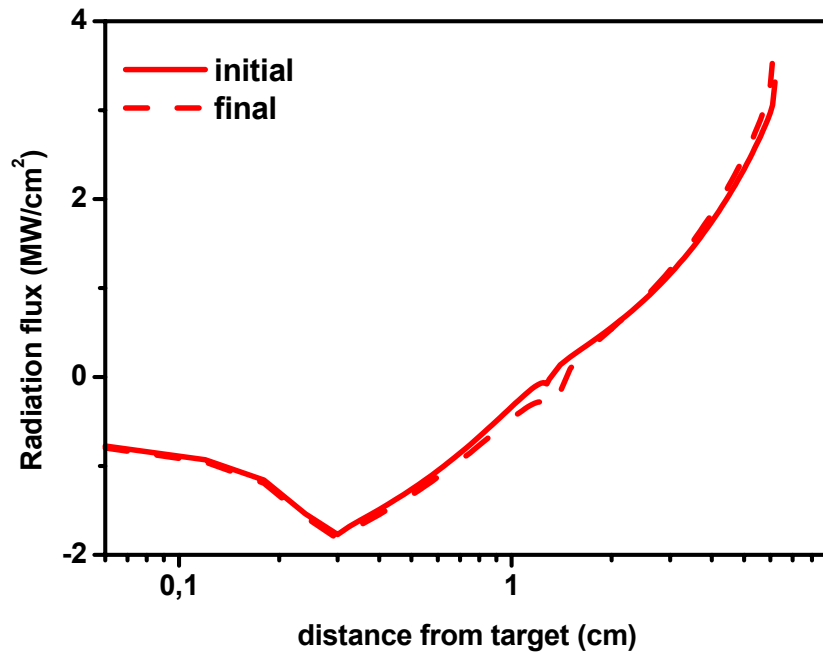


Fig. 27. Total radiation flux calculated for the second test variant (initial and final after 15 iterations) by use of two level model.

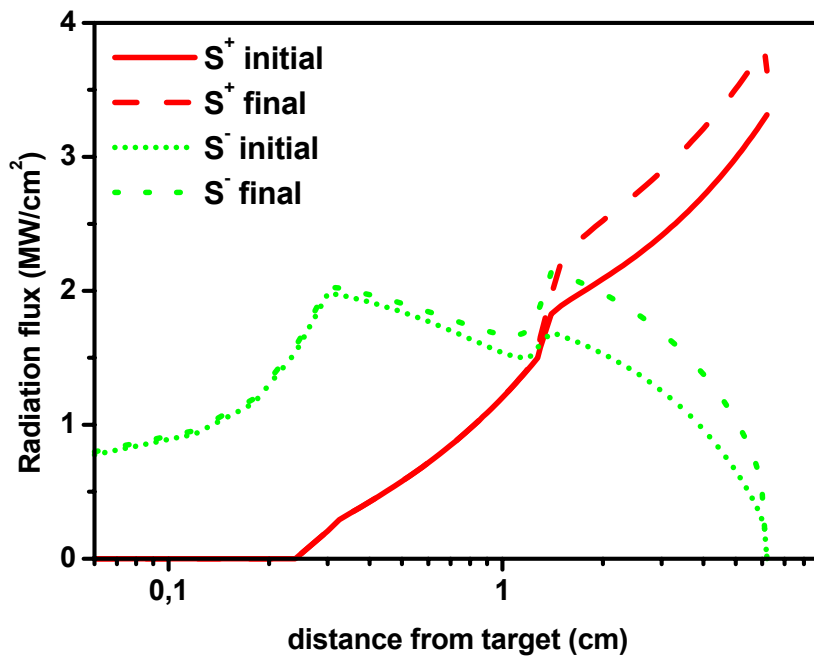


Fig. 28. Radiation flux in positive ($\mu > 0$) and negative ($\mu < 0$) directions for the second test variant (initial and final after 15 iterations) by use of the two level model.

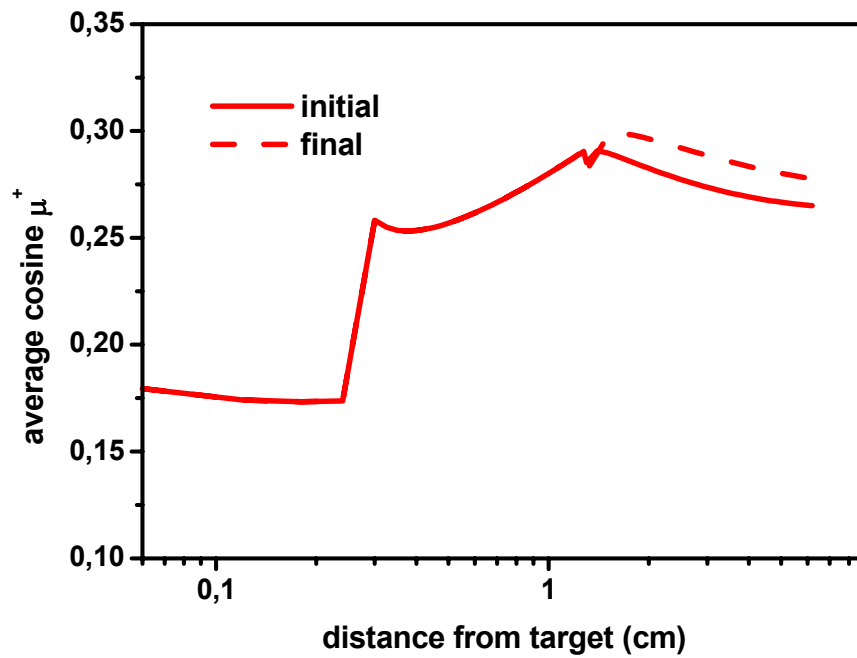


Fig. 29. Average cosine in positive direction ($\mu > 0$) for the second test variant (initial and final after 15 iterations) by use of the two level model.

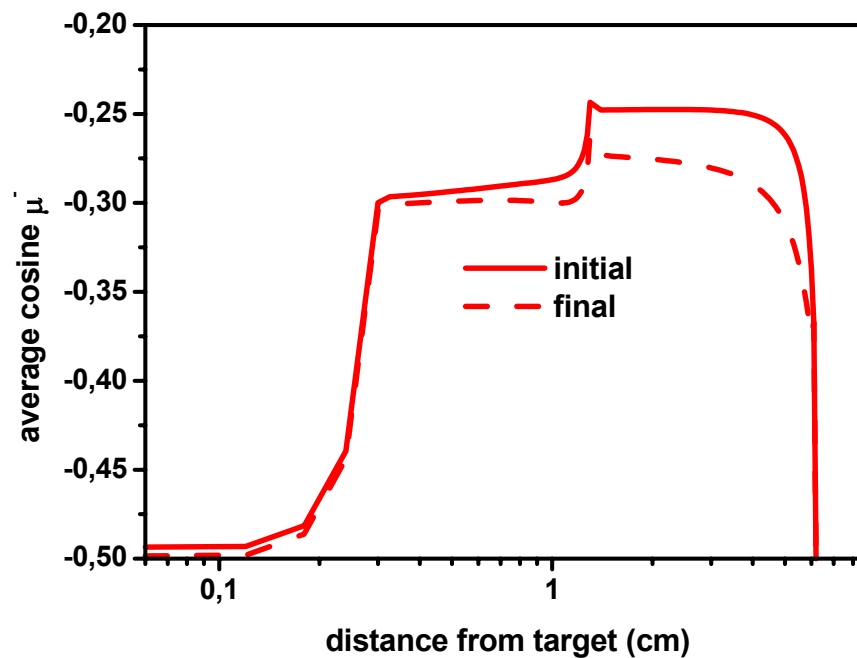


Fig. 30. Average cosine in negative direction ($\mu < 0$) for the second test variant (initial and final after 15 iterations) by use of the two level model.

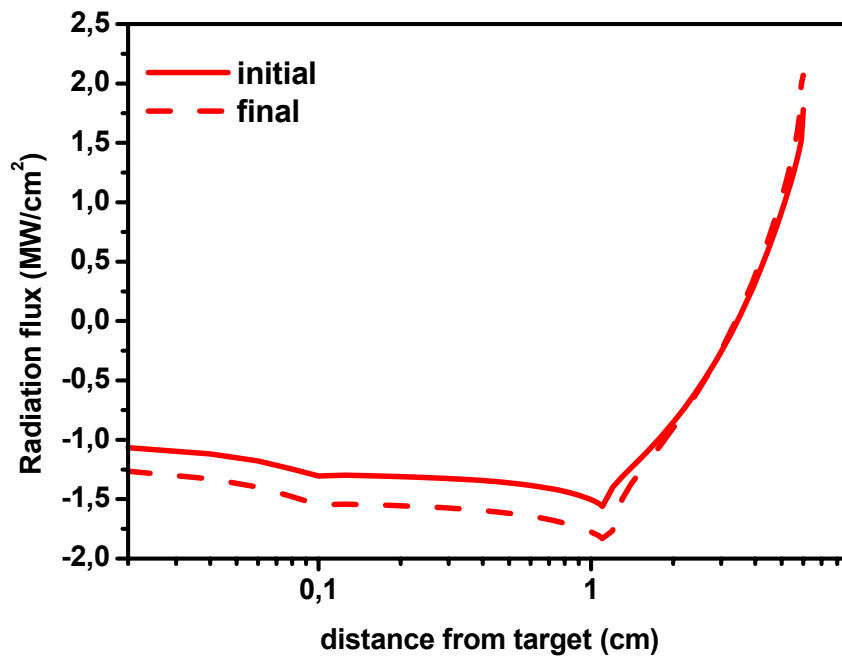


Fig. 31. Total radiation flux calculated for the third test variant (initial and final after 15 iterations) by use of the two level model.

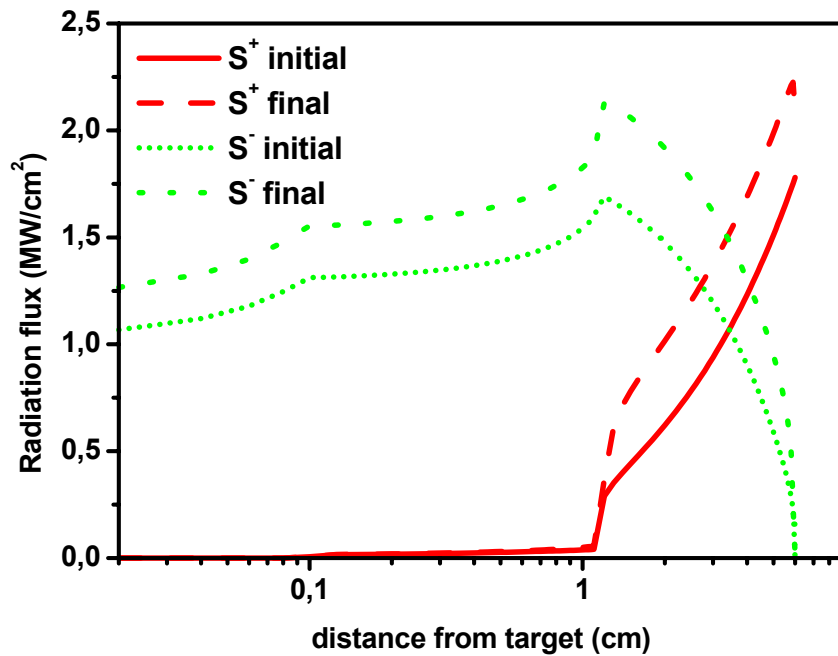


Fig. 32. Radiation flux in positive ($\mu > 0$) and negative ($\mu < 0$) directions for the third test variant (initial and final after 15 iterations) by use of the two level model.

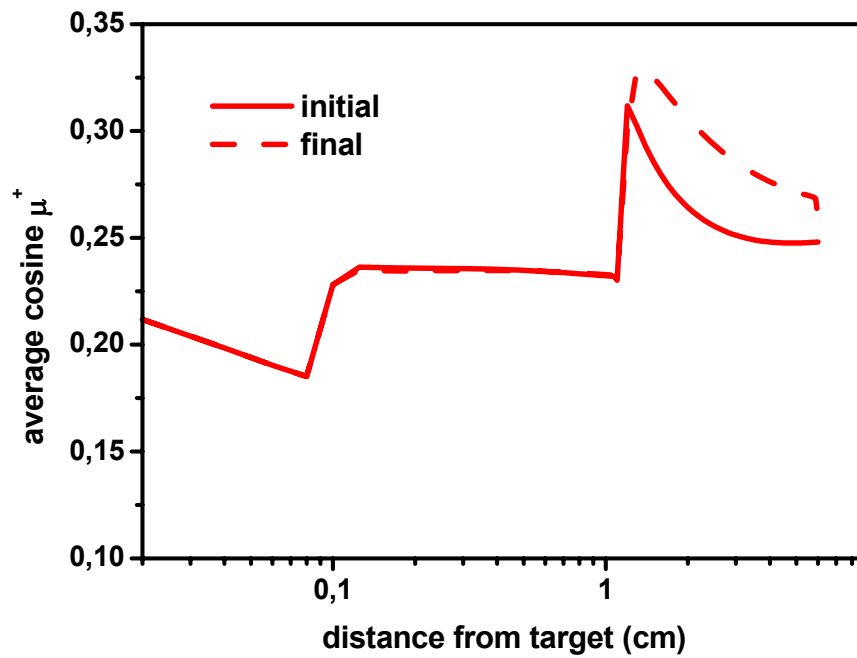


Fig. 33. Average cosine in positive directions ($\mu > 0$) for the third test variant (initial and final after 15 iterations) by use of the two level model.

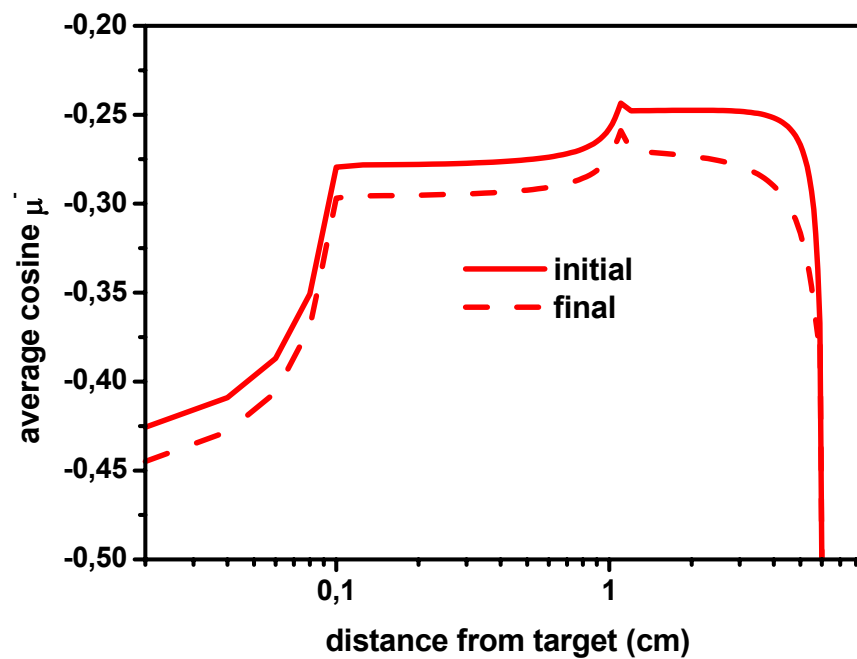


Fig. 34. Average cosine in negative direction ($\mu < 0$) for the third test variant (initial and final after 15 iterations) by use of the two level model.

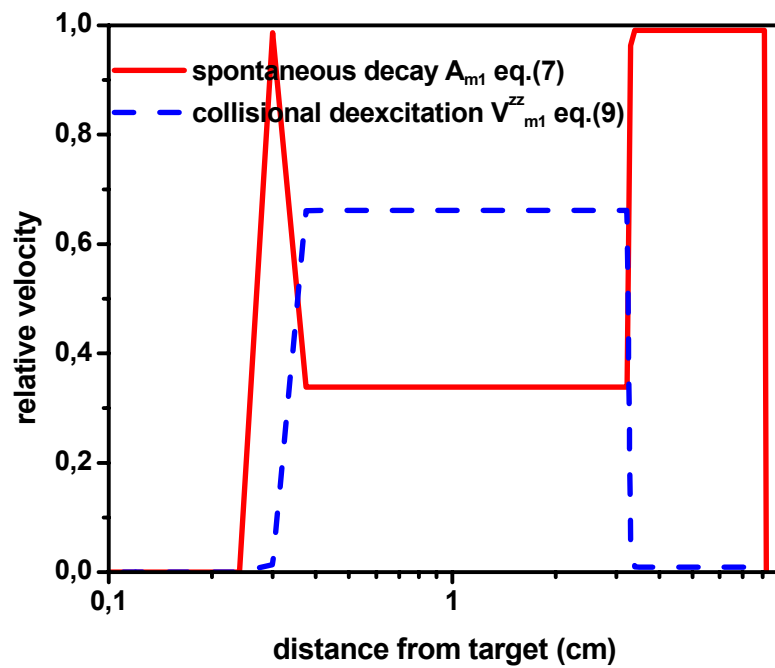


Fig. 35. Relative velocities of decay of excited electrons for the first test variant.

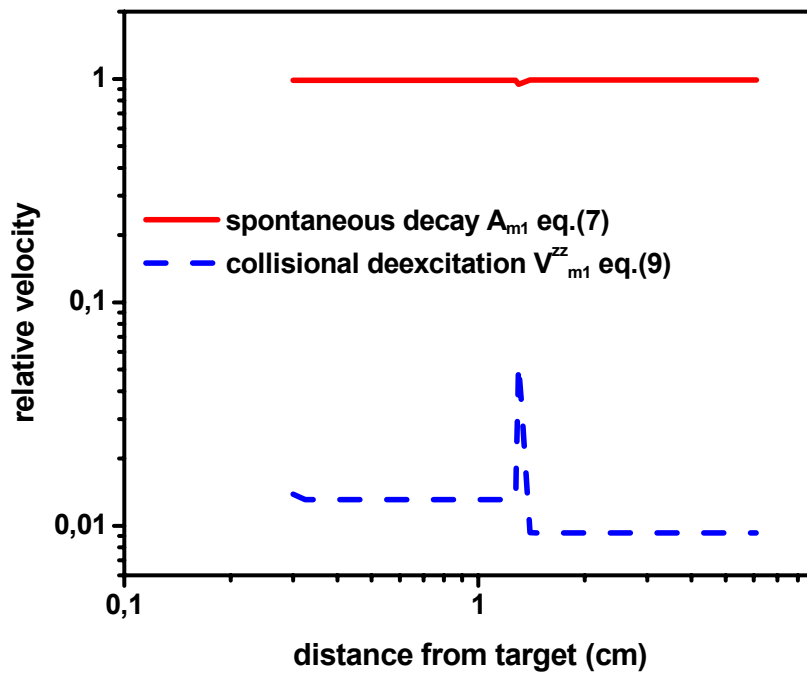


Fig. 36. Relative velocities of decay of excited electrons for the second test variant.

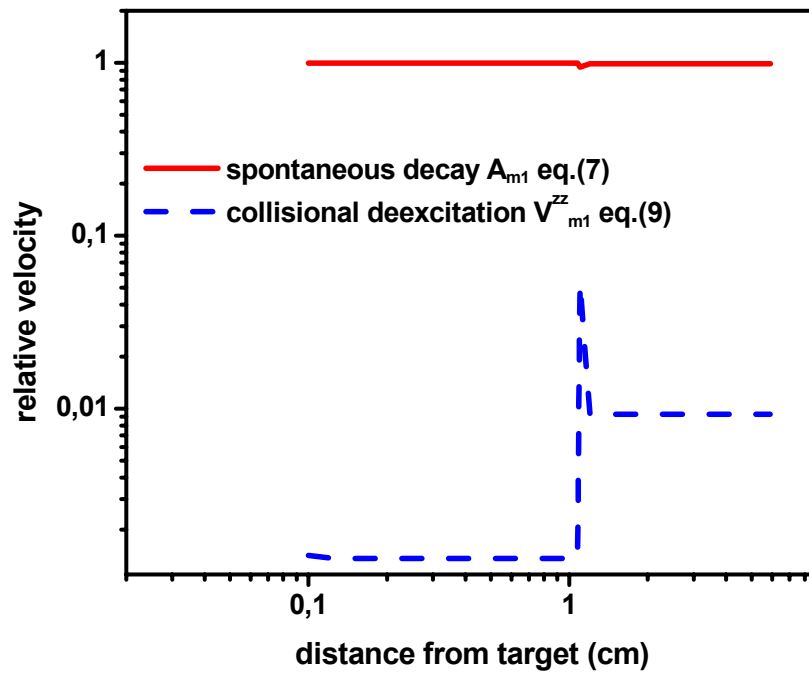


Fig. 37. Relative velocities of decay of excited electrons for the third test variant.

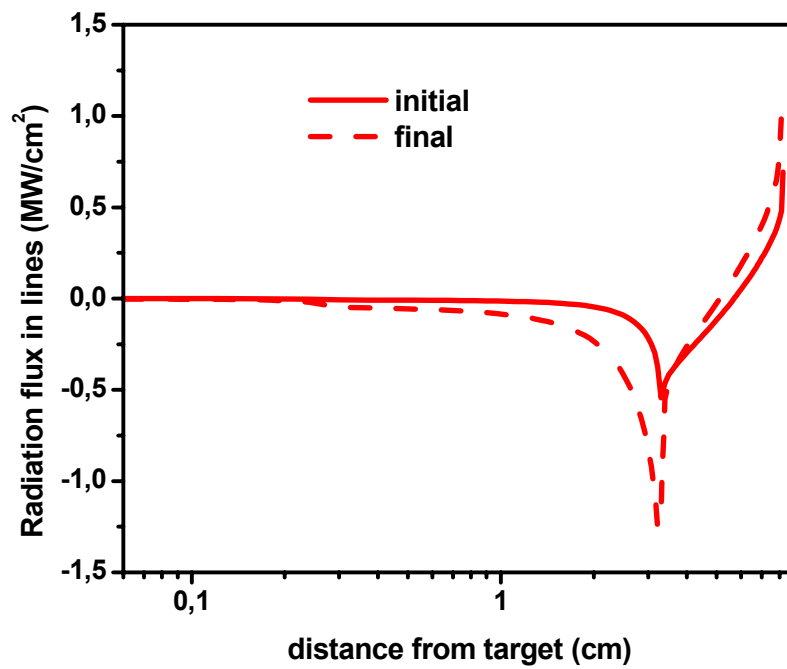


Fig. 38. Radiation flux in lines calculated for the first test variant (initial and final after 15 iterations).

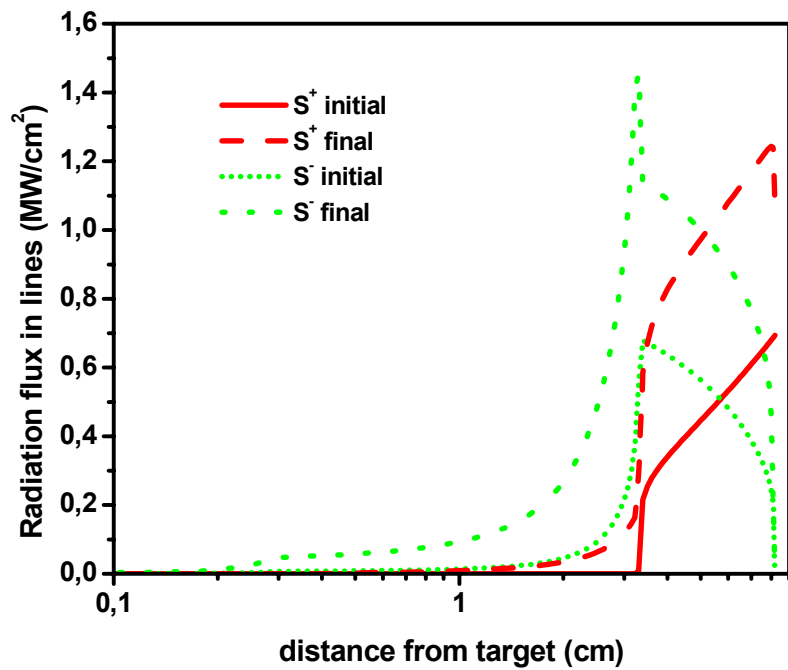


Fig. 39. Radiation flux in lines for positive ($\mu > 0$) and negative ($\mu < 0$) directions for the first test variant (initial and final after 15 iterations).

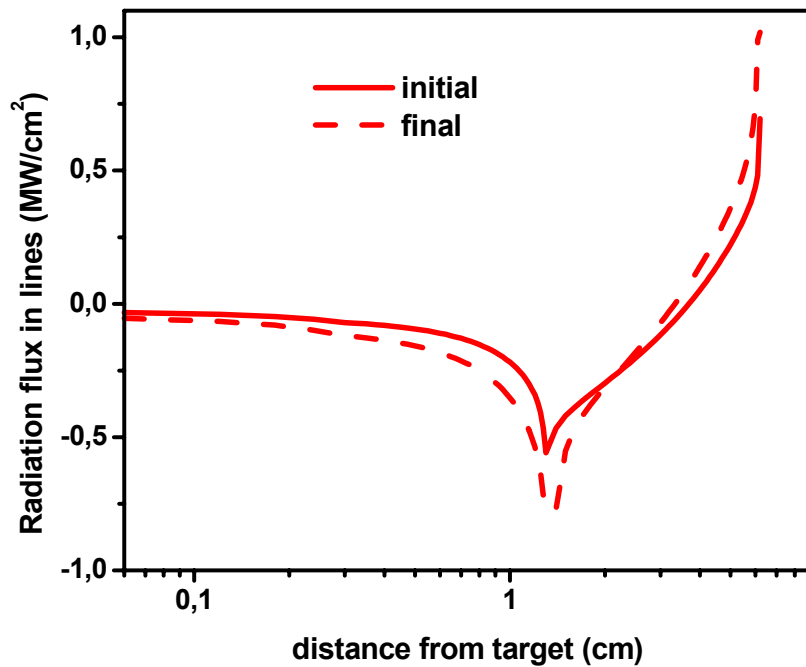


Fig. 40. Radiation flux in lines calculated for the second test variant (initial and final after 15 iterations).

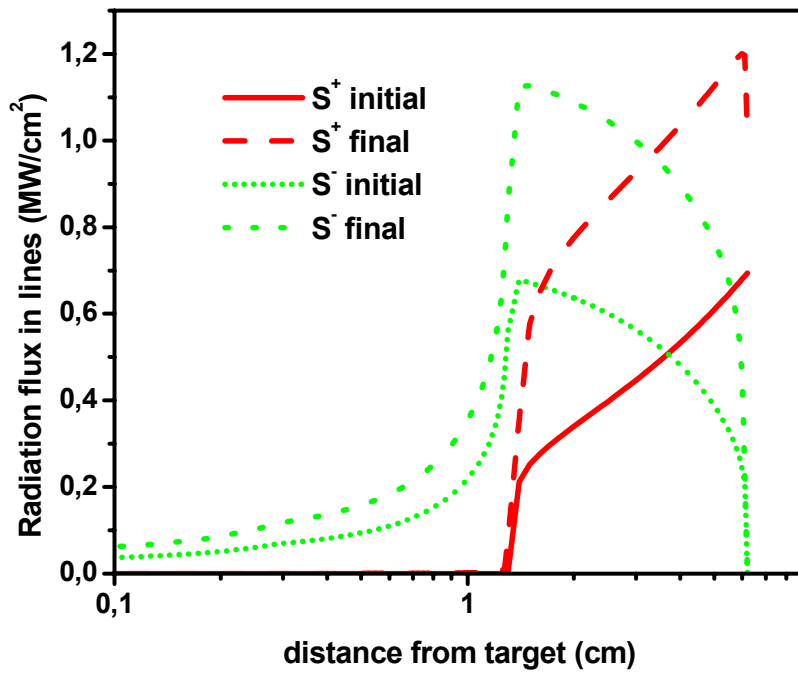


Fig. 41. Radiation flux in lines for positive ($\mu > 0$) and negative ($\mu < 0$) directions for the second test variant (initial and final after 15 iterations).

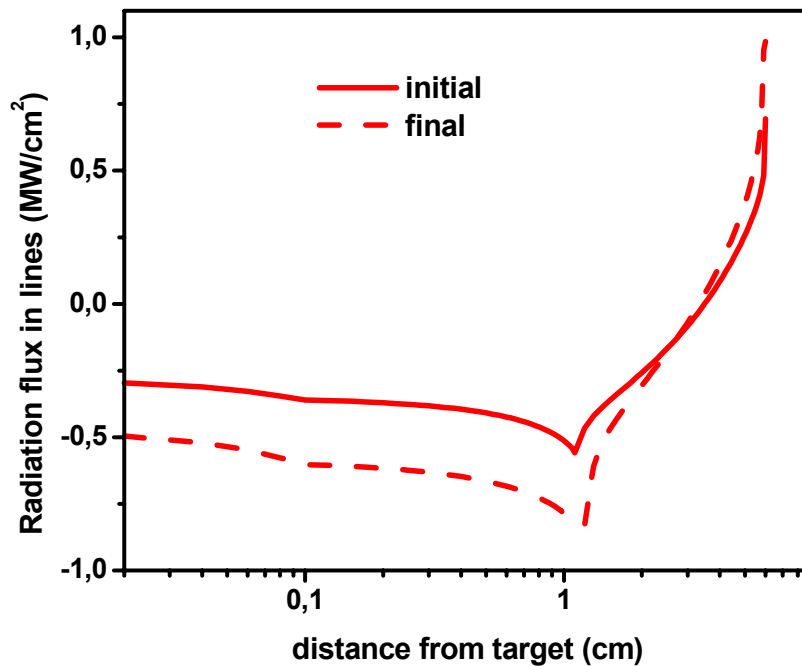


Fig. 42. Radiation flux in lines calculated for the third test variant (initial and final after 15 iterations).

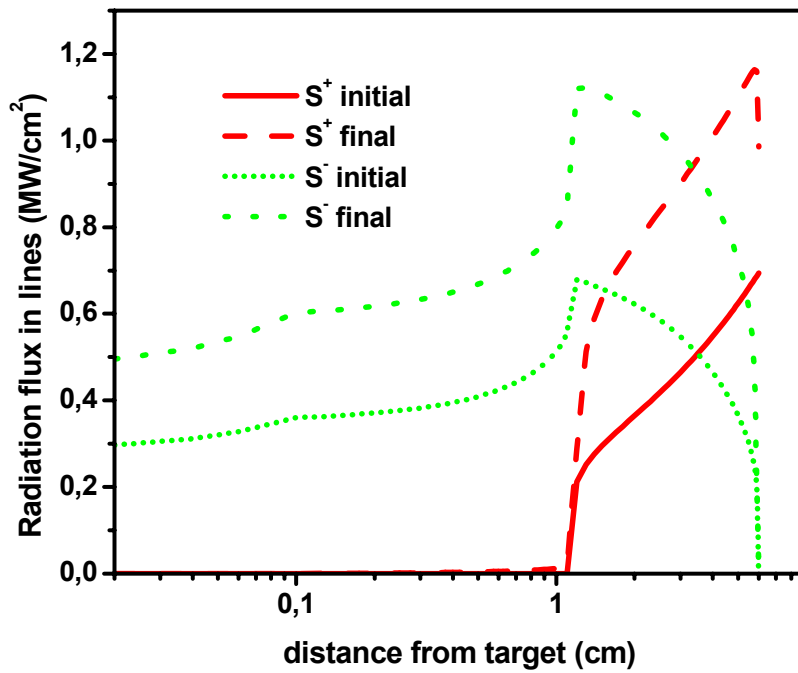


Fig. 43. Radiation flux in lines for positive ($\mu > 0$) and negative ($\mu < 0$) directions for the third test variant (initial and final after 15 iterations).

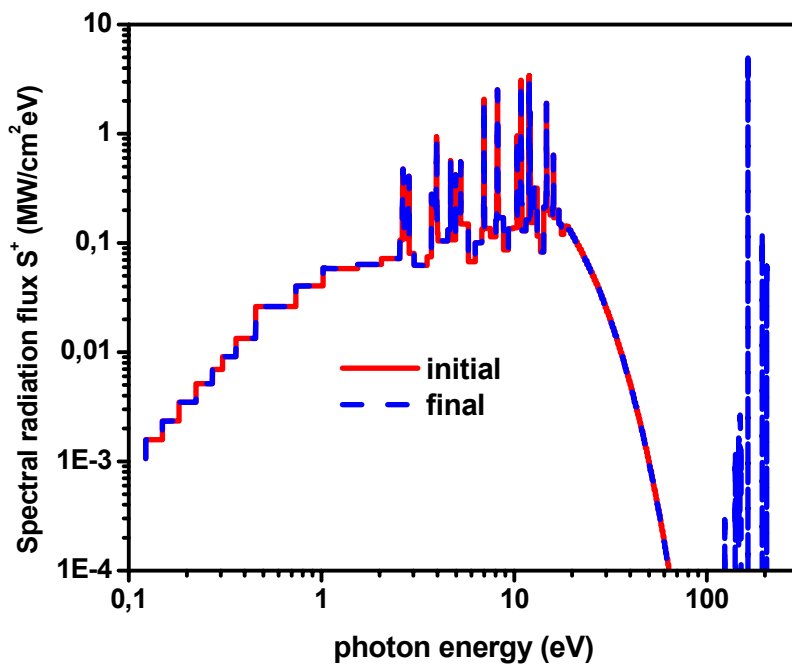


Fig. 44. Typical spectral radiation flux in positive ($\mu > 0$) direction at position $x=3.2$ cm for the first test variant (initial and final after 15 iterations).

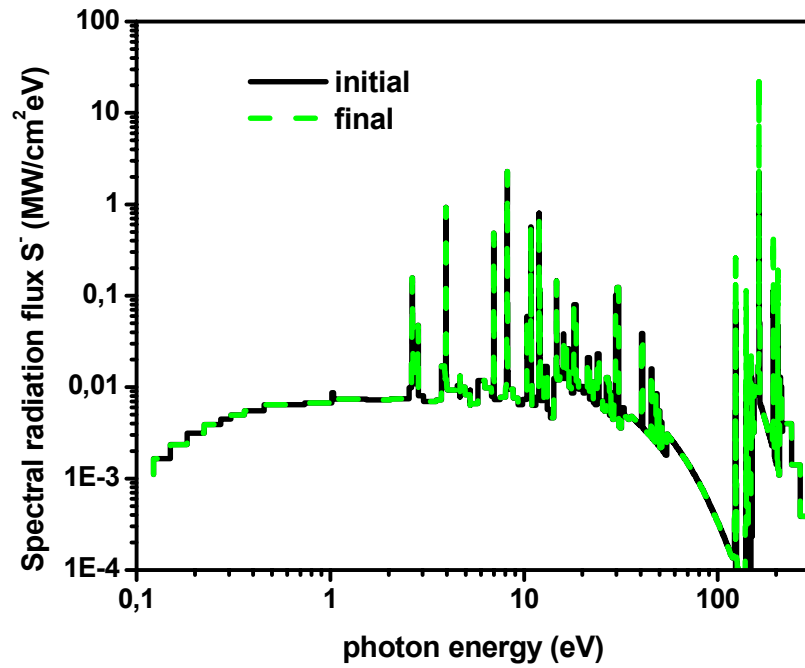


Fig. 45. Typical spectral radiation flux in negative ($\mu < 0$) direction at position $x=3.2$ cm for the first test variant (initial and final after 15 iterations).

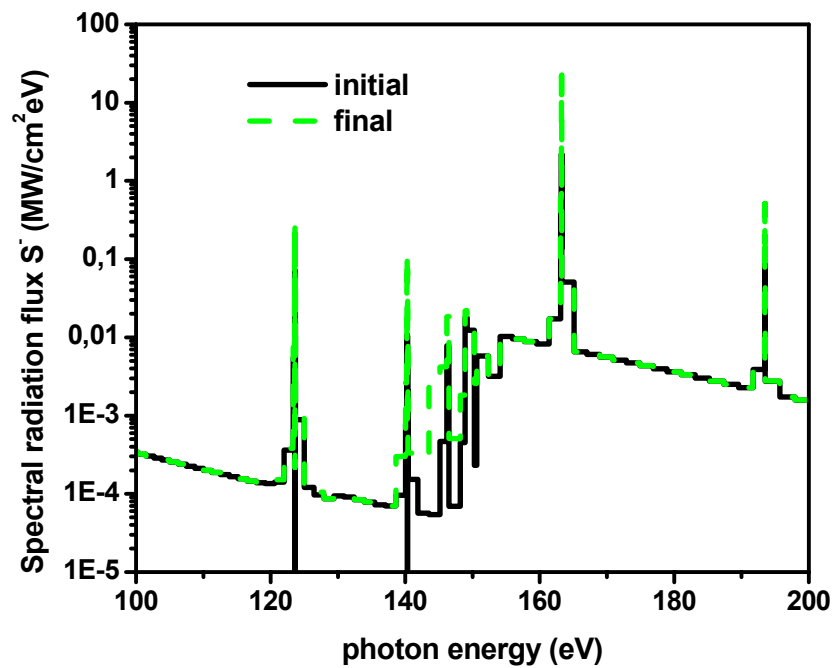


Fig. 46. Typical spectral radiation flux (in SXR range) in negative ($\mu < 0$) direction at position $x=3.2$ cm for the first test variant (initial and final after 15 iterations).

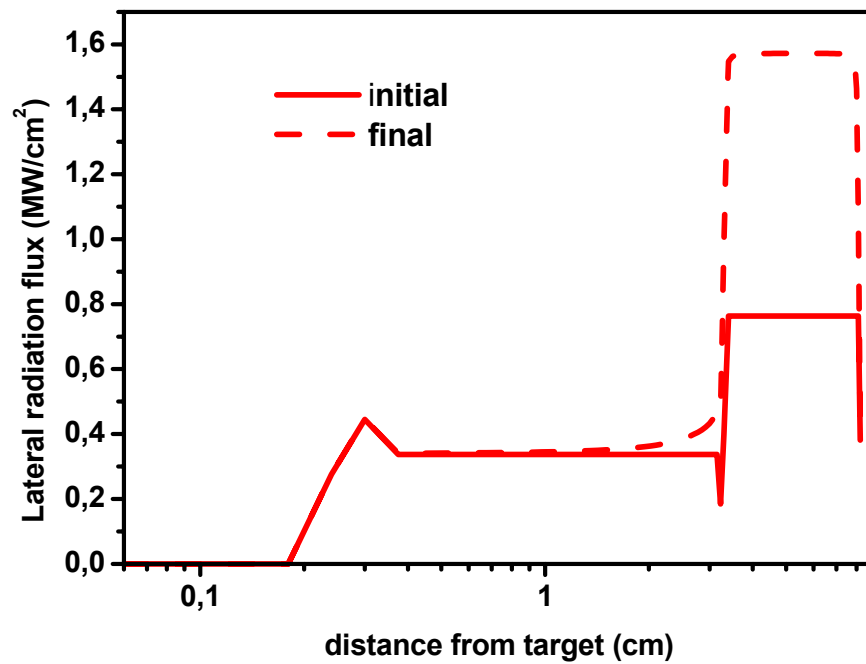


Fig. 47. Angular integrated lateral leakage radiation flux in lines calculated for the first test variant (initial and final after 15 iterations).

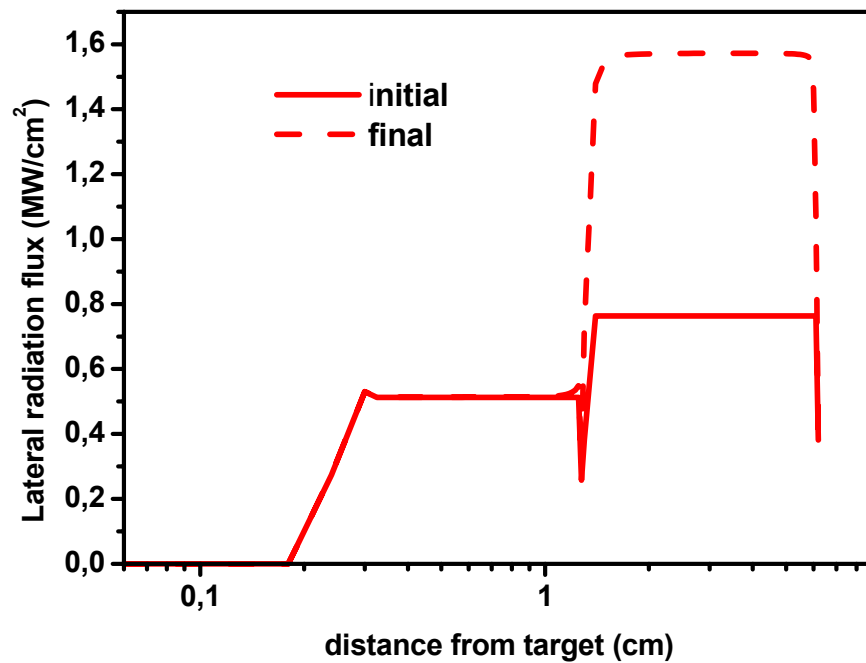


Fig. 48. Angular integrated lateral leakage radiation flux in lines calculated for the second test variant (initial and final after 15 iterations).

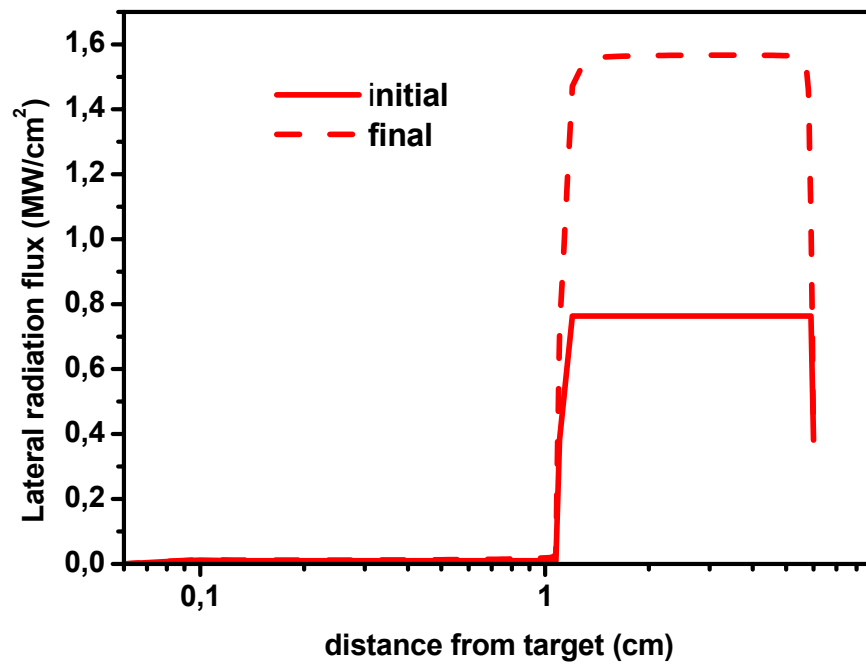


Fig. 49. Angular integrated lateral leakage radiation flux in lines calculated for the third test variant (initial and final after 15 iterations).

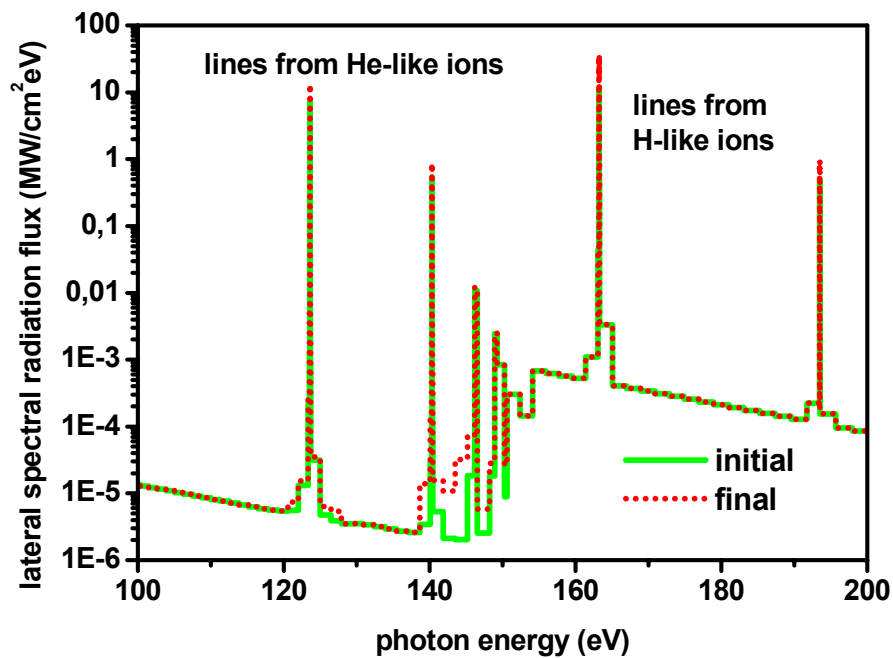


Fig. 50a. Typical lateral leakage spectral radiation flux in the SXR range, showing the lines from He- and H-like ions for the first test variant at a distance of $x=4$ cm from the target.

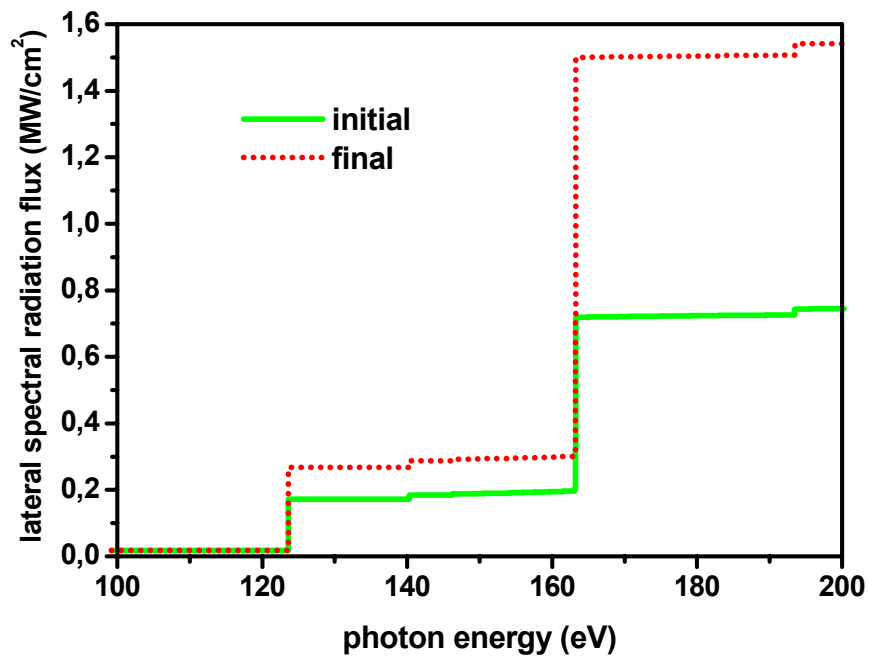


Fig. 50b. Integrated lateral leakage radiation flux showing the contributions from the line radiation for the first test variant at a distance of $x=4$ cm from the target.

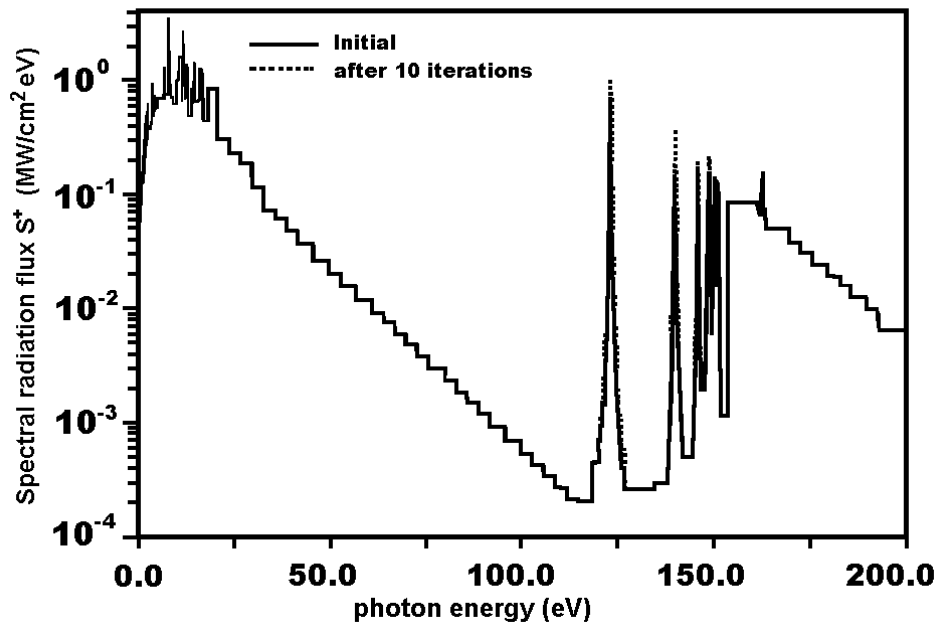


Fig. 51. Calculated back radiated spectral flux using the fixed profile from Figs. 4,5.

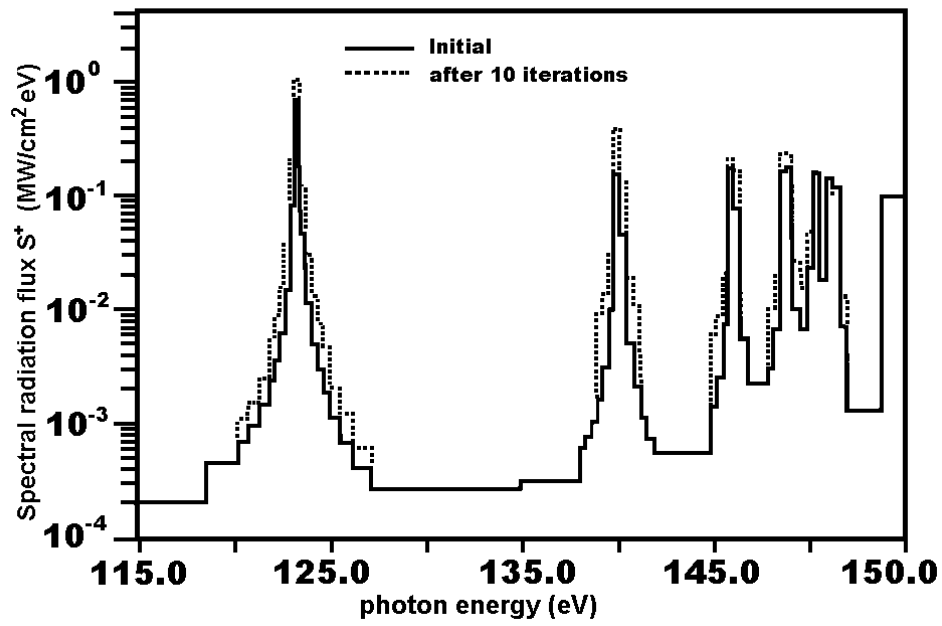


Fig. 52. Calculated back radiated spectral flux in a narrow spectral range.

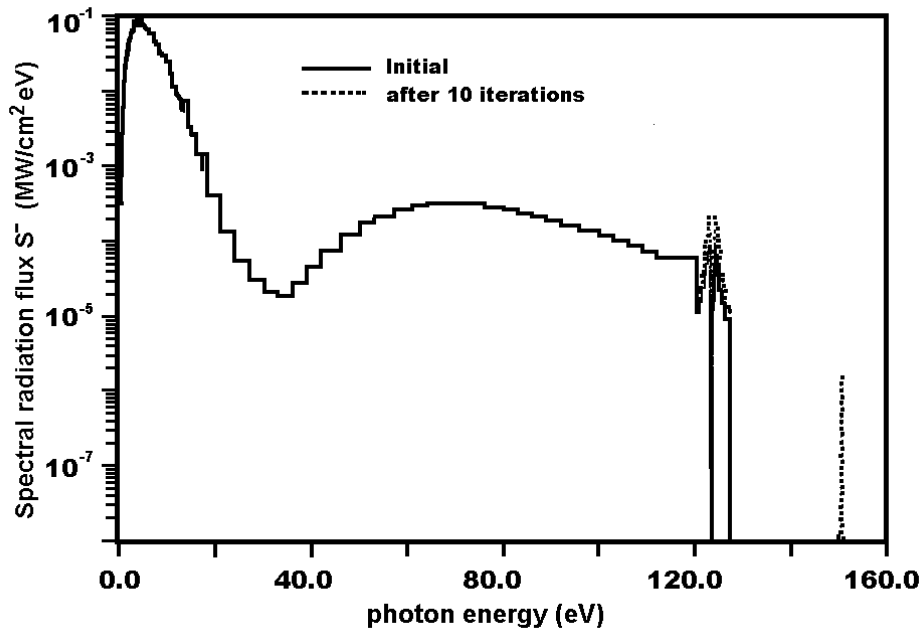


Fig. 53. Spectral radiation flux to the target, calculated for fixed profile from Figs. 4,5.

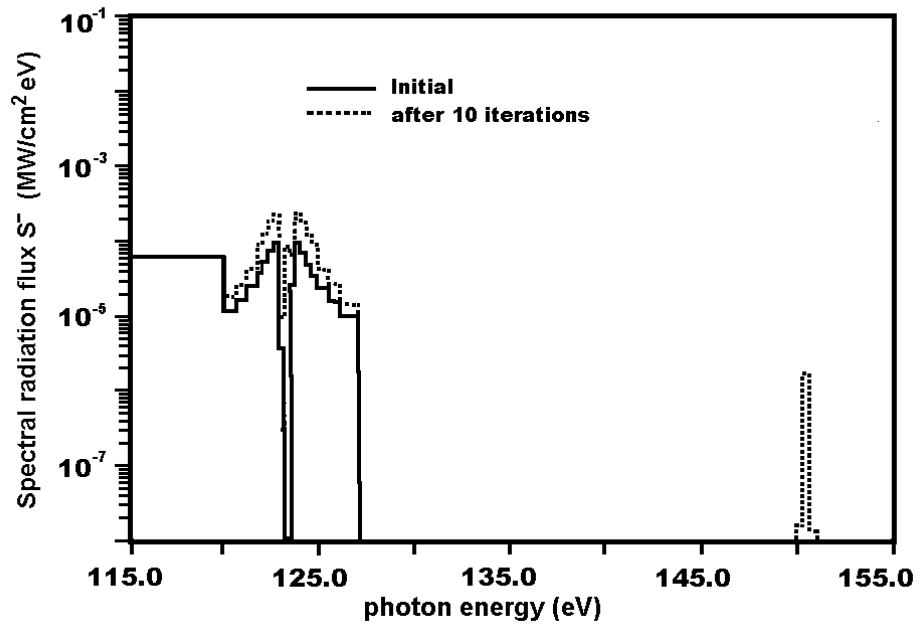


Fig. 54. Spectral radiation flux to the target in a narrow spectral range.

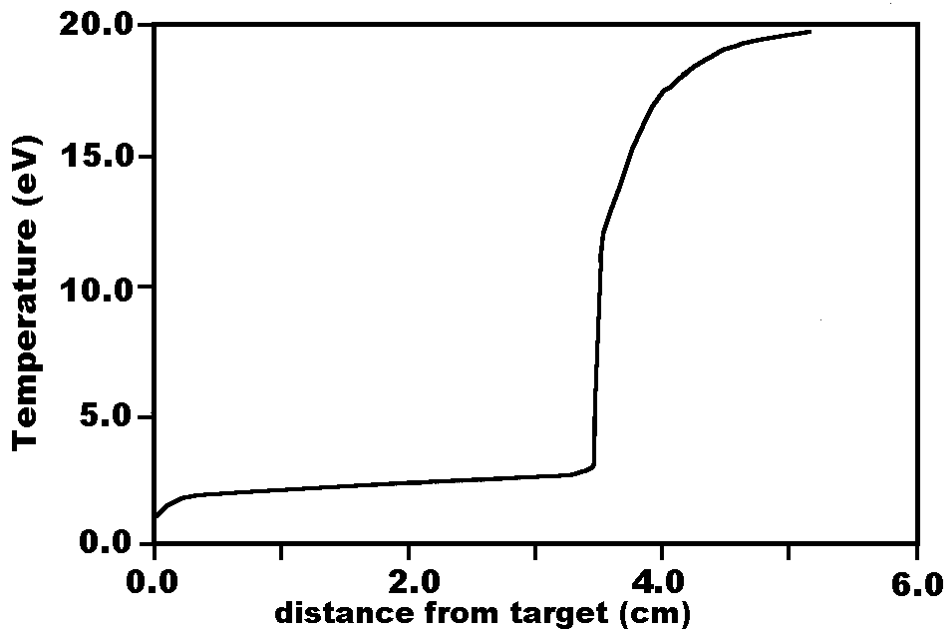


Fig. 55. Typical temperature profile for a beryllium plasma shield.

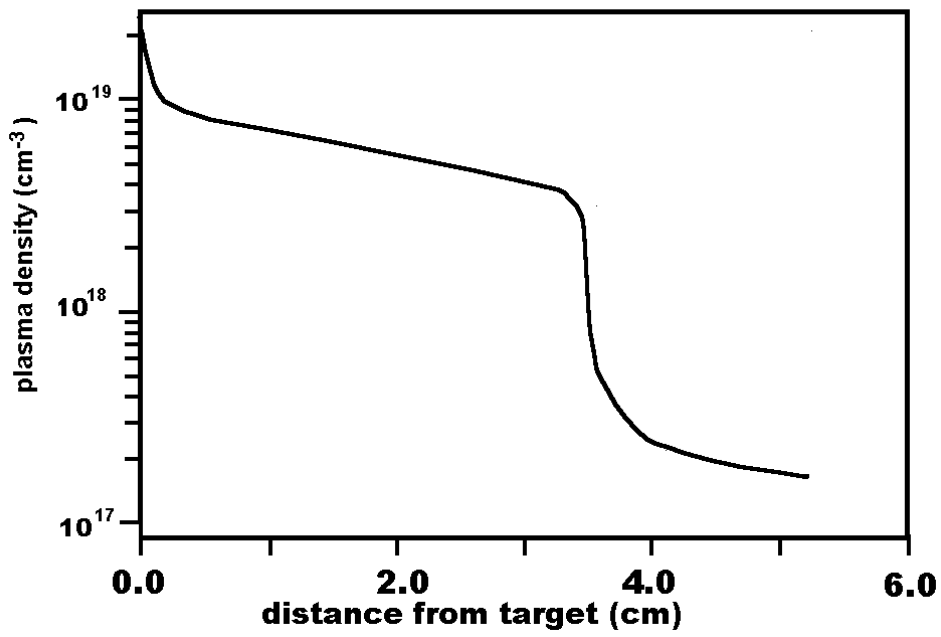


Fig. 56. Typical density profile for a beryllium plasma shield.

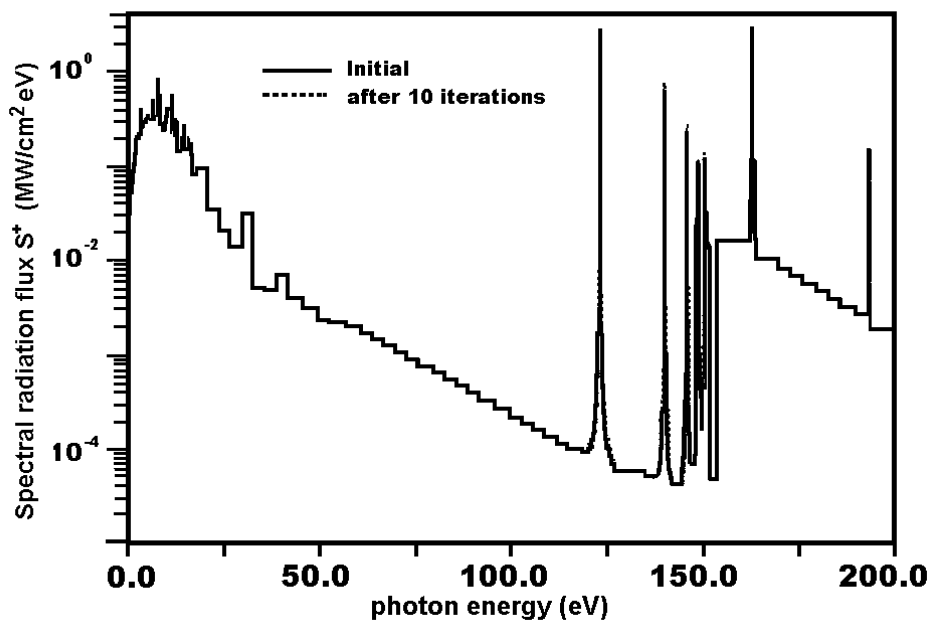


Fig. 57. Back radiated spectral flux, calculated for the fixed profile from Figs.55,56.

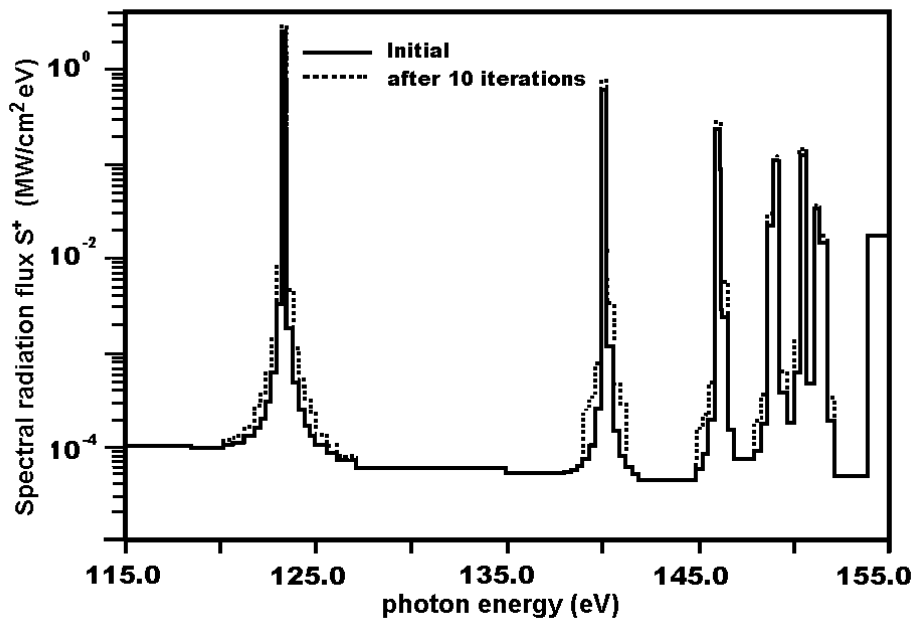


Fig. 58. Back radiated spectral flux in a narrow spectral range.

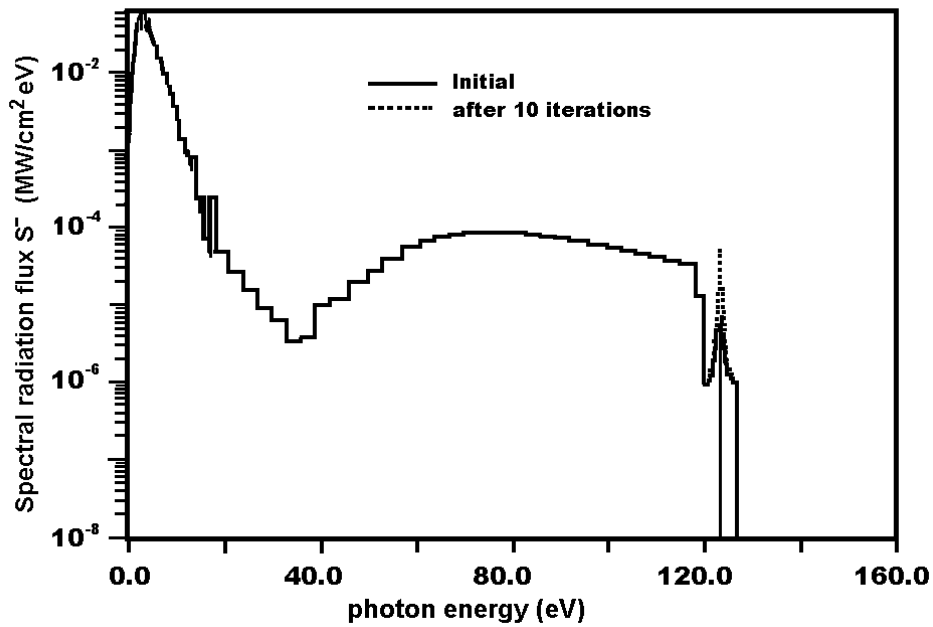


Fig. 59. Spectral radiation flux to the target, calculated for fixed profile from Figs.55,56.

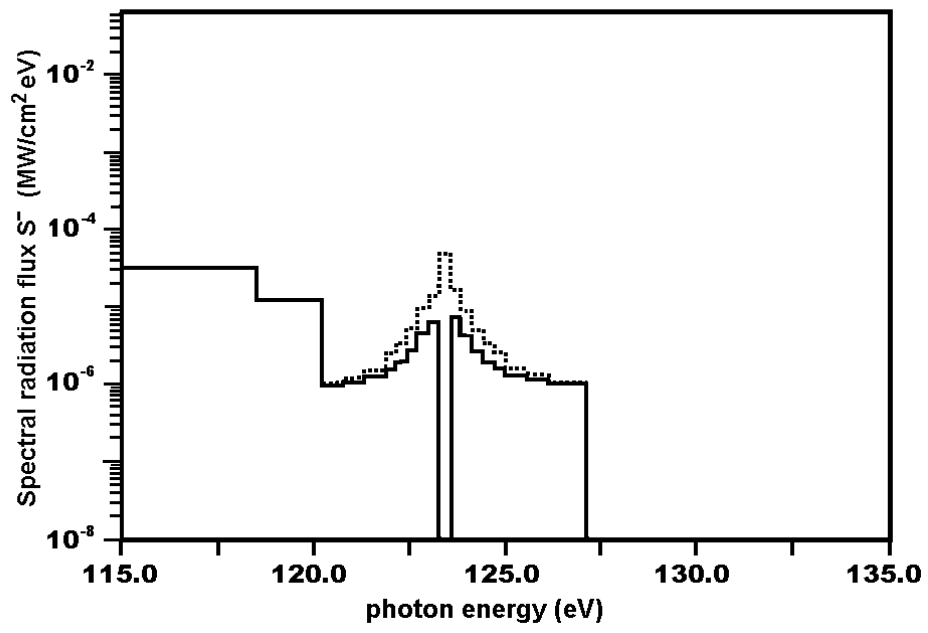


Fig. 60. Spectral radiation flux to the target in a narrow spectral range.